Magnetostratigraphy of the Mercia Mudstone Group (Devon, UK): implications for regional relationships and chronostratigraphy in the Middle to Late Triassic of western Europe.

***Mark W. Hounslow[1,2] and Ramues Gallois[3]**

1. Lancaster Environment Centre, Lancaster University, Lancaster, UK. LA1 4YW
2. Earth, Ocean and Ecological Sciences, Univ. of Liverpool, Jane Herdman Building, Liverpool, L69 3GP; mark.w.hounslow@gmail.com; orcid. ID: 0000-0003-1784-6291
3. 92 Stoke Valley Rd., Exeter EX4 5ER, UK gallois@geologist.co.uk orcid ID:0000-0001-5925-576X

Abstract: Global synchronisation of environmental change in terrestrial successions in deep-time is challenging due to the paucity of dating methods, a case also applicable to the Middle to Upper Triassic Mercia Mudstone Group in Britain. Using coastal cliff sections, magnetostratigraphy was evaluated at 263 horizons, defining 53 magnetozones. Magnetozones from the lower 140 m of the group demonstrate correspondence to those from the mid Ladinian to early Carnian polarity timescale, dating which is compatible with magnetostratigraphy from the underlying Sherwood Sandstone Group. Magnetostratigraphy of the Dunscombe Mudstone Formation, and associated palynological data, suggest a late Carnian to earliest Norian age, and a dramatically lower accumulation rate than adjacent formations. The polarity record demonstrates coeval flooding events, evaporite deposits and intervals of sand supply between the Wessex Basin and the Central European Basin in the Carnian. This is the result of linked climatic and eustatic changes between these separate basins, related to aeolian dust supply and the shrinkage of hyper-arid source regions for the fines. Magnetostratigraphy from the Branscombe Mudstone and Blue Anchor formations demonstrates their Norian and early Rhaetian age. These and other data suggest an alternative synchronization of marine and non-marine polarity records for the Norian polarity timescale.
198 words

Supplementary material: Section details and detailed logs of the sampled sections and inferred sequence boundaries, magnetic mineralogy data, demagnetisation behaviour and mean directions, summary of virtual geomagnetic pole data and a comparison to other European poles, construction of other composite reference sections and revised polarity

scales. Excel sheet of magnetic data statistically evaluated correlation models, and age models.

Accurate and precise dating of sediment successions is the cornerstone of global understanding of many past environmental changes in deep time. It is particularly challenging merging datasets from terrestrial successions into such understanding, because of the common lack of detailed, accurate and precise biostratigraphies. In Europe the Middle and Late Triassic contains rather contrasting intervals of environmental change. The Middle Triassic saw the marine flooding of the Central European Basin (CEB) from the Palaeotethys Sea, through gateways on its southern borders (McKie 2017). Faunal and floral turnovers were low during the Middle Triassic (Brayard et al. 2009; Song et al. 2018). During the Carnian, the start of the Late Triassic, major environmental changes are linked to a northern-hemisphere-focused humid episode (Ruffell et al. 2016), which is associated with the diversification of the dinosaurs (Bernardi et al. 2018). The transition into the Norian witnessed major turnovers in marine biota (Dal Corso et al. 2020), linked to significant fluctuations in sea-water temperature, which later in the Norian witnessed rising temperatures and a climax in reef-building in the Palaeotethys (Sun et al. 2020).

In Britain the Mercia Mudstone Group (MMG) occupies part of the Middle (Ladinian Stage) and most of the Upper Triassic (Carnian to Rhaetian stages), which is ~36 Myr in duration, representing 72% of the Triassic (Ogg et al. 2020). However, the chronostratigraphy of the MMG is poorly understood, so synchronisation of environmental signals encoded in these red-bed sediments has remained elusive. The type section of the MMG is on the Devon coast and lies within the Dorset and East Devon Coast World Heritage Site (Gallois 2019). The MMG sections on the Devon coast are among the best exposed and accessible Middle and Upper Triassic sedimentary rocks in Europe. The MMG contains palynological assemblages recorded from two intervals, which allow a loose biostratigraphic age assignment to parts of the Carnian and Rhaetian (Warrington 1997; Hounslow et al. 2004; Baranyi et al. 2019). Other intervals are barren, hence the detailed chronostratigraphy of the remainder of the MMG is unknown. On the Devon coast the MMG rests on the Middle Triassic Otter Sandstone Formation (Fm), with the age of its upper part based on magnetostratigraphy and vertebrate fossils, thought to be Anisian in age (Benton et al. 1994; Benton 1997; Hounslow and McIntosh 2003). The current work addresses the age of the MMG using magnetostratigraphy, which allows the importation of chronostratigraphy by correlation with conodont and ammonoid dated successions elsewhere, that contain a linked magnetostratigraphy. This provides better insight into synchronisation of environmental changes with elsewhere in Europe.

The MMG was also important in the early development of palaeomagnetism, with geomagnetic reversals first detected in this unit in the pioneering study of Clegg et al. (1954). Expanding on preliminary work of Creer et al. (1954), the details of the first magnetostratigraphy from Triassic age sediments was by Creer (1959) from a 52 m section across the Otter Sandstone Fm - MMG boundary east of Sidmouth, in which three magnetozones were identified. Also pioneering was the use of alternating field tumbling demagnetisation on sediments which was later followed by a pioneering study using low-temperature methods to characterise the magnetic mineralogy of red beds (Creer 1961).

Currently, the Middle and Late Triassic geomagnetic polarity timescale (GPTS) is reasonably well understood allowing international chronostratigraphic correlations to be established (Gallet et al. 2007; Hounslow and Muttoni, 2010; Maron et al. 2019; Zhang et al. 2020; Ogg et al. 2020). However, the magnetic polarity pattern in some parts of the Carnian is less certain (Zhang et al. 2020; Hounslow et al. 2022a). In the Upper Triassic uncertainty remains about an internationally agreed position for the base of the Rhaetian (Galbrun et al. 2020), although that for the base of the Norian is closer to formal acceptance (Hounslow et al. 2021b).

We determined a magnetostratigraphy from the Devon coastal outcrops, providing the first detailed chronostratigraphy of the MMG. This provides a better understanding of the synchronisation of the British Middle and Upper Triassic with respect to the much better studied German Triassic. These data also allow re-assessment of the composite polarity timescale through the Norian by using additional data from the Upper Chinle Formation (of New Mexico and Arizona) and elsewhere. This suggests a revised GPTS that shows better convergence of the astronomically scaled magnetostratigraphy from the Newark Supergroup and biostratigraphically better-dated marine sections through the Norian-Rhaetian.

The Mercia Mudstone Group in the Wessex Basin

The sections exposed in the east Devon cliffs between the outfall of the River Sid [SY 129 873] at Sidmouth, and east of the outfall [SY 273 893] of the River Axe at Seaton provide the type section of the Mercia Mudstone Group (Howard et al. 2008; Gallois, 2019 Fig. 1). A total of about 470 m of Mercia Mudstone Group sediments, predominantly red mudstone (and some green) with a few thin beds of sandstone, are exposed in these sections. There are minor gaps in the succession due to faulting with potentially larger gaps in the Axe Valley Fault Zone (Fig. 1). Micro- and macro-fossils are largely absent in these mudstones.

The MMG was previously inferred to range in age from the early Ladinian to late Rhaetian based on: a) Anisian-age vertebrates (Benton et al. 2002) and a magnetostratigraphy from the underlying Otter Sandstone Fm (Hounslow and McIntosh 2003), b) Carnian miospores from the predominantly green and grey mudstones in the Dunscombe Mudstone Fm (DMF) and immediately adjacent units (Baranyi et al. 2019) and c) Rhaetian miospores from the Lyme Regis Borehole (Warrington 1997) and miospores and magnetostratigraphy from the top-most Branscombe Mudstone and Blue Anchor formations in the Bristol Channel Basin (Hounslow et al. 2004).

The MMG comprises four formations and eight members (Gallois 2001) that crop out in almost continuous coastal cliffs between Sidmouth and Seaton (Fig. 1; Table 1). Detailed lithological logs and magnetostratigraphic sampling points for the sections between Sidmouth and Haven Cliff are shown in the Supplementary Information (SI Figs. S1.1 to S1.7).

The red mudstones that make up most of the MMG are thought to have formed largely in arid playa environments, with mud input likely via mud-pellets (Talbot et al. 1994; McKie 2017), and/or loess accumulation (Jefferson et al. 2000; Mao et al. 2021). In more marginal situations in the north-eastern part of the Bristol Channel Basin some horizons have pedogenic features such as slickensides (Milroy et al. 2019). However, palaeosols are not present in most of the MMG on the Devon coast but do occur within the Dunscombe Mudstone Fm (DMF) and its immediately underlying unit. Sedimentological evaluation of the DMF indicates it formed in a freshwater lacustrine environment with shallow channels (Porter and Gallois 2008), with associated beds of halite/sulphate collapse breccias (Gallois 2003). Within this general pattern of sedimentation there are regional lithological variations that are poorly understood in the absence of age-diagnostic indicators. However, overall facies are like those of other Germanic-type facies in western Europe (Aigner and Bachman 1989; Reinhardt and Ricken 2000; Vollmer et al. 2008; McKie 2017). The Wessex Basin in which these strata accumulated is a sag basin without bounding faults (Butler, 1998). Coeval Upper Triassic basin-margin strata (carbonates and some coarse clastics) onlap basement, with limited areal occurrence, in marginal units to the NW (Milroy & Wright, 2000; Milroy et al. 2019). This basin therefore is tectonically quiescent in contrast to some other well studied Upper Triassic basins, such as the Newark Rift Basin, where tectonism played a more active role in sedimentation (Withjack et al. 2013).

Sampling and Methods

Samples were collected from 262 horizons, including four from the Pennington Point Member (which overlap the sampling of Hounslow and Mcintosh (2003) from the Otter Sandstone Fm). From these samples, 447 specimens were measured (Table 2), placed onto sub-sections that represent natural continuously exposed segments of the MMG outcrop (see SI section 1). Red mudstone horizons were preferred for sampling, if available, but non-red lithologies were sampled in the DMF and Blue Anchor Formation (BAF). Sampling used exclusively oriented hand-samples, prepared from suitable exposures, using hammers and digging tools to expose a fresh block. Flat surfaces on these were oriented with a magnetic compass and a specially designed 'foot-print' orientation staff (Hounslow et al. 2022b). Samples were wrapped in the field for protection during transportation. Sampling was segmented into subsections detailed in Table 2 and SI section S1.

In the laboratory, specimens were re-oriented and set in dental plaster, from which cubic palaeomagnetic specimens were cut dry with a diamond saw (the mudstones tend to fracture and crumble when exposed to saw coolant water).

Low field magnetic susceptibility (K) was measured using either an AGICO Kappabridge or Bartington MS2 meter. Measurements of Natural Remanent Magnetisation (NRM) were made using a 3-axis CCL GM400 cryogenic magnetometer (noise floor ~ 0.002 mA/m with holder correction). Red mudstone specimens were subjected to stepwise thermal demagnetisation, using a Magnetic Measurements Ltd, MMTD1 thermal demagnetiser, in 100-50°C steps up to 720°C, with most steps above 400ºC. Magnetic susceptibility measurements were performed after each heating step, to monitor mineralogical changes caused by the heating, which were mostly minor (see SI). Some non-red samples from the DMF and BAF (41 specimens in total) were measured by a combination of thermal demagnetisation up to around 300-400 ºC followed by reverse-tumbling AF demagnetisation (on a Molspin demagnetiser). This procedure was used to limit thermal alteration which obscured the characteristic remanent magnetisation (ChRM) in these lithologies. The specimen demagnetisation results were analysed using principal component analysis in the LINEFIND software (Kent et al. 1983), to extract the Triassic ChRM from the specimen data (See Hounslow and McIntosh 2003; Hounslow et al. 2008a; 2021a for analysis details). Great circle type behaviour was also shown by many specimens during demagnetisation, and behavioural classes S (for linear -fits) and T (great circle behaviour) were assigned to specimens (see demagnetisation behaviour panel in Figs 2 to 7). These were further sub-

divided into three qualitative classes (S1, S2, S3 and T1, T2, T3; with class 1 the top quality) based on the directional scatter and number of points in the fitted principal component data (see Hounslow et al. 2008a; 2021a for classification details). Directional data for some of the weakest intensity specimens was too erratic and these specimens were rejected (X-class). Based on the approach to expected Triassic directions and the behaviour classes, the specimen is assigned a polarity quality (R, R?, R??, ?, N??, N? or N), to indicate its reversed or normal polarity status, with R? or N? indicating a polarity assignment of lower quality, compared to R or N of top quality. '?' indicates the specimen could not be confidently assigned a polarity (Figs. 2 to 8).

The specimen virtual geomagnetic pole (VGP_R) latitudes (Hounslow et al. 2022b), were determined with respect to the reference mean VGP direction for either the Sidmouth Mudstone (MS, MD samples), Dunscombe Mudstone (MW samples), Branscombe Mudstone (ML, SH, MB, SE samples) or Haven Cliff (HC samples) data. Values of VGP_R latitude near $+90^o$ indicate a normal polarity specimen and values near -90^o indicate reverse polarity (Figs. 2 to 8). Directional statistics (see SI Table S3.1) were determined with PMagtool v.5 (Hounslow 2006).

The magnetic mineralogy of the red mudstones of the Sidmouth Mudstone Fm was described by Creer (1957, 1961), and additional data are given in SI section 2, confirming haematite dominates the natural remanent magnetisations (NRM) in most of the MMG.

Statistical t of the magnetic polarity correlations was determined by firstly characterising the polarity pattern in terms of five metrics for each magnetozone, t_0, $\log_e(t_{-1}/t_0)$, polarity bias, Shermans ω_2 statistic and geometric mean. Where t_0 is the thickness (or duration) of the magnetozone, and t_{+1}, t_{-1} are the corresponding values for the underlying and overlying magnetozones. The later three metrics use t_{+1}, t_0 and t_{-1}. $\text{Log}_e(t_{-1}/t_0)$ is used in quantitative polarity correlation since it is less dependent on sedimentation rate changes (Man, 2008; Lallier et al. 2013). The polarity bias, ω_2 and mean thickness metrics characterise more about the local polarity structure than using t_0 or $\log_e(t_{-1}/t_0)$ individually (Olsen et al. 2014) and have been used in quantitative multivariate polarity correlation (Hounslow et al. 2022b). Using these metrics for each magnetozone the polarity correlation models were evaluated for statistical similarity using the similarity of matrices index (SMI) and Procrustes similarity index (PSI) using methods in Indahl et al. (2018), The probability of association of the corresponding polarity patterns uses the RV-based statistic P_{RV} (Josse et al. 2007). Lastly the divergent characteristics of each magnetozone in the correlation models was

characterised by the Euclidean distance (d_i) using the above five metrics above, in which more problematic intervals of correlation are highlighted with larger d_i. Care was taken to approximately normalise the five metrics to similar means and standard deviations. This involved using $\log_e(t_{-1}/t_0)*0.5$ and $2*\omega_2$ and most-often scaling magnetozones to duration (in Myr). This allows comparison of the median of d_i (d_{median}), as an additional approximate measure of overall polarity pattern divergence. Statistical comparisons used R.

We also provide a preliminary assessment of the sequence stratigraphy of the MMG, which is used with an assessment of the wider regional implications of this study. Details of sequence boundaries selected are indicated in SI Table S1.2. These use the playa-lacustrine environmental models proposed by Aigner and Bachman (1989), Reinhardt and Ricken (2000) and Vollmer et al. (2008).

Results

NRM intensity is broadly related to colour, with red-mudstones having intensity 1-7 mA/m, and others 0.03- 1.5 mA/m (left panels in Figs. 2 to 8). The multi-coloured lithologies from the DMF have a less simple relationship to NRM intensity (Figs. 4a; see SI section 2). Demagnetisation behaviour shows two components: a low laboratory unblocking temperature (LT) component and a dual polarity ChRM at the highest unblocking temperature. The LT component typically ranges from NRM or 100 ºC to around 350ºC, but in some specimens can extend to 500ºC or more rarely to 600ºC (See SI section 3). The LT component typically dominates the magnetisation, which rapidly demagnetises in intensity towards 400 ºC (SI section 2). The Fisher mean of the LT component (in geographic coordinates) is 349°, +53° (α_{95}=5.9°, k=3.3, n=245) and may be partly a Brunhes-age component, but with many specimens displaying partial overlap with the Triassic components (see SI section 3 for details and demagnetisation plots). However, the mean inclination is shallower than expected for the Brunhes (~67°), indicating the LT component could be partly acquired during the Early Cretaceous, when the MMG were eroded and onlapped (Fig. 1).

The ChRM in red mudstones is shown predominantly by linear fits to the high temperature steps (on average from 480 ºC to 680-700 ºC or the origin; see SI section 3), but with some more unusual specimens having ChRM that unblocks from 150-400 ºC. In the non-red lithologies from the DMF, ChRM ranges are 300-400ºC to 40 - 80mT or the origin. Linear fits comprise data from 62% of specimens (S-class data points in Figs. 2 to 8, 255 specimens). The ChRM identified by great circle trends toward the expected direction (T-

type behaviour; Figs. 2 to 8), comprised 32% of specimen data (133 specimens). The remaining 6% of specimens failed to yield useful directional data either due to complete LT and ChRM component overlap or absence of a ChRM (indicated as X-class). A total of 88% of specimens were assigned polarity using the two better categories of polarity quality (i.e. N, R, N?, R?).

Mean directions were determined for each section using either the S-class directions (Fig. 9) or additionally using the great circle data from the T-class specimens (SI Table S3.1). Directions mostly pass the reversal test with class Rb or Rc, and the derived palaeopoles are like other Triassic poles from stable Europe (see SI section 4).

Magnetostratigraphy

Magnetozones are assigned to 12 major magnetozone couplets labelled SS1 to SS12 (Sidmouth to Seaton composite section), with SS12 in the Seaton Cliff section. The basal reverse magnetozone in the MMG is labelled BS8r, continuing the labelling used by Hounslow and McIntosh (2003) for the Budleigh Salterton to Sidmouth sections in the Sherwood Sandstone Group (Fig. 2). The Haven Cliff section uses a separate magnetozone code (HC1n to HC3r; Fig. 8) because its relationship with the SS-magnetozones is less secure.

The lower ~140 m of the MMG between the River Sid outfall to Hook Ebb (Figs. 2,3) is composed of 11 magnetozones, with the thickest magnetozone (SS1n) in the whole of the group at 36 m, in the Salcombe Hill Mudstone Mb (Fig. 2). The polarity in the top of the Otter Sandstone Formation (Pennington Point Mb) east of Sidmouth is consistent with that previously measured in the same interval west of Sidmouth by Hounslow and McIntosh (2003), and their correlated data are also shown on Fig. 2. Some larger sampling gaps are present in the Hook Ebb Mudstone Mb (Fig. 3), and three of the magnetozones are defined by single samples (2 specimens each; SS2r.1n; SS3n.1r) in the Salcombe Mouth to Hook Ebb section (Fig. 3). Polarity data of Creer (1959) from the lower part of this section identifies the base of a normal polarity magnetozone some 17 m above a green sandstone level, which is presumably near the top of the Otter Sandstone, and normal polarity below the sandstone level, with an intervening reverse magnetozone some 17-22 m thick. These polarity changes are like our data, but reverse magnetozone (BS8r) is some double the thickness of Creer's. Lithological logs were not given by Creer (1959), so either; a) these differences relate to a thickness error, or b) the upper part of BS8r in Creer's data was too strongly overprinted by

261 the LT overprint, that AF demagnetisation at 120 mT (and 3 years storage in zero field) failed
262 to remove it.
263 The SS1n-SS3r polarity boundary coincides with the basal sandstone bed in the base
264 of the Salcombe Mouth Mb, indicating there could be a hiatus at this level. Similarly, the
265 SS2r-SS3n polarity boundary coincides with a halite breccia bed so it could be there is a
266 hiatus between samples MD1 and MD4 across this ~1 m breccia interval.
267 The 45 m of section at Strangman's Cove preserves 18 magnetozones, with three
268 additional tentative reverse magnetozones in the upper part of the Little Weston Mudstone
269 Mb (SS3n.2r, SS3n.3r, SS3n.4r; Fig. 4). This part of the Little Weston Mudstone Mb was one
270 of the least well exposed parts of the MMG (at the time of sampling), and the sparser
271 sampling probably inadequately represents the polarity changes. The high sampling density in
272 the lower and mid parts of the DMF indicates frequent reversals, or a relatively condensed
273 interval in the MMG. The Lincombe Sandstone Mb (a lenticular siltstone/sandstone body if
274 evaluated using adjacent outcrops) is exclusively reverse polarity (SS4r; Fig. 4). The change
275 in polarity across the base of the Lincombe Sandstone Mb could indicate a hiatus at its base.
276 Likewise, the halite breccias in the section likely indicate a hiatus in the section at these
277 levels (Fig. 4). An interval at -2.5 m with slickensides (Fig. 4) is a probable palaeosol. This
278 occurs in an interval of strata that is infrequently exposed in the upper part of the Little
279 Weston Mudstone Mb (172 -183 m in composite height; SI Fig. S1.3).
280 The stratigraphically higher but partially overlapping 45 m section at Littlecombe
281 Shoot west displays dominantly reverse polarity with a single-sample normal magnetozone in
282 the lowest Littlecombe Mudstone Mb (SS8r.1n; Fig. 4). Samples from the upper sandstone
283 are of reverse polarity (magnetozone SS9n.1r; Fig. 5) embedded in a thicker normal polarity
284 magnetozone SS9n, which extends into the base of the section at Littlecombe Shoot east (Fig.
285 5a). The magnetostratigraphy in the Littlecombe Shoot Mb may be more complex than the
286 sampling indicates, because seven of the submagnetozones in this member are based on only
287 single samples (but 2 specimens from each, e.g., basal part of SS9r; Fig. 5).
288 The section between Red Rock and Branscombe Mouth starts in reverse magnetozone
289 SS9r (Fig. 6), like the upper-most sampled part at Littlecombe Shoot east, but passes up into
290 normal polarity (SS10n, SS11n), which is dominant in the mid and upper parts of this section
291 (Fig. 6). Two submagnetozones are defined by a single sample, one at the base of the Seaton
292 Mudstone Mb (SS9r.3n), and one at ~48 m above the base of the Seaton Mudstone Mb
293 (SS11n.1r; Fig. 6).

The Seaton Cliff section is dominated by normal magnetozone SS12n, but with three submagnetozones defined by single samples (SS12n.1r, SS12r.1r, SS12r.1n; Fig. 7).

The Haven Cliff section has well defined magnetozones, particularly those in the uppermost Seaton Mudstone Mb and throughout the Haven Cliff Mudstone Mb where sampling density is higher (i.e., HC2n; Fig. 8). The specimens from the BAF were challenging to measure and analyse due to the weak NRM intensity (many <0.1 mA/m), larger directional scatter, and dominance of great-circle type behaviour (Fig. 8). Four magnetozones are defined by a single sample, with multiple specimens (HC1n.1r, HC1n.2n, HC2n.1r and HC3r.1n), and three tentative submagnetozones (HC2n.2r, HC3n.1r, HC3r.2n; half width bars in polarity column; Fig. 8) are defined by a single specimen. One sample has specimens of opposite polarity and is assigned unknown polarity (grey bar at -11 m; Fig. 8).

Overall, the MMG magnetostratigraphy has a moderate number of magnetozones defined by single samples (21 out of the total), which is a non-ideal situation, and could be rectified with detailed sampling of sparse intervals.

Discussion and synthesis

Timing issues in red-bed magnetisations

The fine-grained haematite (the pigment) which colours many red-bed successions generally has been generated over-long time intervals by oxic diagenesis. This pigment component often largely carries the overprint magnetisations or it is sufficiently fine-grained to acquire no persistent remanence. The specularite (haematite generally > 1μm in size) in red beds is responsible for the stable magnetisations either produced during deposition, during very early burial, or in some cases during longer-term diagenesis, like the pigment (see reviews by Butler, 1992 and Swanson-Hysell et al. 2019). Some of the issues connected with the ‘red-bed controversy’, which was most active in the late 1970-1980’s, were also related to the incomplete demagnetisation methods (i.e. blanket demagnetisation) often employed at the time, which were unlikely to separate primary from secondary components and later diagenetic-related magnetisations. These have now been superseded by more complete demagnetisation approaches. It is clear from the work of Creer (1959, 1961) that the MMG contains both pigment and specularite. Likely, the LT component in the MMG is largely carried by the pigment, as evidenced by the often-rapid intensity decay during thermal demagnetisation and unblocking of this component (see SI). Isolation of magnetisations in

randomly tilted intraformational intraclasts is the classic way to test for specularite components acquired prior to deposition (Swanson-Hysell et al. 2019). Intraclasts are rare in the MMG (and only of small size), so this method cannot be easily applied.

We infer that the ChRM in the MMG red-sediments is largely carried by detrital haematite deposited during deposition (or close to that time). This is based on: 1) The ChRM is carried by both haematite and magnetite in the DMF, which contains both normal and reverse polarity intervals. The DMF red mudstones appear little different magnetically to other parts of the MMG. 2) The ChRM directions are of dual polarity with palaeopoles much like many other European Triassic sediments; 3) Magnetisations are simple in directional behaviour, unlike those inferred to be acquired over long-term intervals which tend to be more complex (Butler, 1992). 4) Magnetozones are straightforward to define, without many single-sample polarity intervals, which could be a characteristic of patchy diagenetic production of specularite.

However, it cannot be excluded that some of the specularite has been produced over longer time intervals. This could be responsible for the great-circle type behaviour seen in some specimens, so longer-term diagenetic-related magnetisations are not fully separated from near-depositional components when demagnetised. The wide dispersion in the declination of the poles to the great circles for the specimens with t-class ChRM's (SI Fig. S3.2) is consistent with contamination from rather dispersed secondary components, perhaps acquired over longer and variable time-intervals into the Brunhes (e.g., SI Fig. S3.1). Possibly some of the 6% of specimens that retain no ChRM are dominated by magnetisations from pigment or diagenetic specularite.

Age of the Sidmouth Mudstone Formation and international comparisons

Independent constraints on the age of the Sidmouth Mudstone Fm (SMF) are provided firstly by vertebrates, largely from the Chiselbury and Pennington Point members (and some older occurrences from the Otterton Ledge Member) of the underlying Otter Sandstone Fm (Benton et al. 1994; Spencer and Storrs 2002; Gallois 2005; Coram et al., 2017). The key taxon *Eocyclotosaurus* is largely known from the upper parts of the Otter Sandstone (Coram et al., 2017). The age of these vertebrate assemblages has been inferred by comparison to similar assemblages in better dated strata of the Röt Formation (in Germany) and the Holbrook Member (Moenkopi Formation, USA) described by Lucas and Schoch (2002). The Röt Formation in the CEB is early Anisian in age (Nawrocki and Szulc 2000; Szurlies 2007).

From the Moenkopi Formation (in Arizona), magnetostratigraphy from the Holbrook Member suggests it has a late Anisian age range from magnetochrons MT4 to MT7, a correlation also constrained by (CA-TIMS) U-Pb detrital zircon dates (Haque et al. 2021; Fig. 10).

In addition, vertebrate assemblages like those of the Otter Sandstone Fm occur in the Bromsgrove Sandstone of the Midlands, which is inferred to be Anisian (Seyfullah et al. 2013), because the overlying MMG has Anisian age palynomorphs (Benton et al. 1994). In contrast, fish remains from the Otter Sandstone Fm suggest a Ladinian age (Milner et al. 1990). The level of uncertainty in the widely inferred Anisian age for the Otter Sandstone Fm, based on the vertebrates alone is unclear. Indeed, some have emphasized the inherent uncertainties and flaws in the concept of land vertebrate faunachrons and their means of age control (Rayfield et al. 2009; Irmis et al. 2010; Martz and Parker, 2017)

Secondly, age is inferred from miospores in the uppermost SMF, DMF and basal Branscombe Mudstone (Baranyi et al. 2019). Two palynologically-productive samples some 38 m below the base of the DMF in the Wiscombe Park-1 borehole, were assigned to the early Julian Substage (earliest Carnian) by Baranyi et al. (2019), a position some 6 m above the base of the Little Weston Mudstone Mb (Gallois 2007).

The Little Weston Mudstone Mb palynology accords with the normal polarity dominance of this member, which characterises the early part of the Julian (Fig. 10). The underlying magnetostratigraphy from the remainder of the SMF seems a good match to the GPTS in the mid and late Ladinian (Fig. 10). However, there are differences in the presence of brief normal subchrons in MT11r, which are only seen from the Seceda core dataset (Maron et al. 2019; Hounslow and Muttoni 2010). Other marine sections containing MT11r such as Mayerling and Gammsstein-1 only have reverse polarity (Maron et al. 2019), like our data from magnetozone BS8r (Fig. 10). These correlations suggest the base of the SMF closely corresponds with the start of MT11r in the mid Ladinian.

The reverse polarity dominated mid and late Anisian (MT4r to MT8r) is a distinctive polarity feature of the Middle Triassic (Fig. 10). This MT4r-MT8r interval is primarily evidenced by well-dated magnetostratigraphies from the Mushcelkalk (Nawrocki and Szulc 2000), the upper Guandao section (Lehrmann et al. 2015; Li et al. 2018), and the Milne Edwards Fjellet section on Svalbard (Hounslow et al. 2008b). The coeval upper part of this interval (MT7 to MT8r) is also found in other sections from Italy, Greece, Austria, and Svalbard (Hounslow et al. 2008b; Maron et al. 2019). The MT4r to MT8r chron interval is

most likely equivalent to the BS3r to BS6r magnetozones in the Otterton Ledge Mb of the Otter Sandstone Fm (correlation option-1 in Fig. 10). This correlation option gives a fair correspondence between the number and relative thickness of magnetozones in the BS6 to BS8n interval and the two possible GPTS interpretations for this interval. Option-1 (our preferred solution) places the base of the Ladinian close to the base of the Chiselbury Mb of the Otter Sandstone (Fig. 10).

The differences between the GPTS of Hounslow and Muttoni (2010) and Maron et al. (2019) in the MT4r-MT8r interval are due to use of the Guandao section data as the reference section for the lower and mid parts of this interval by Maron et al. (2019). Whereas Hounslow and Muttoni (2010) used more datasets for this interval. Because of the uncertainty in this part of the GPTS, a second possibility is that the MT4r-MT8r interval represents BS3r-BS5r, shown as correlation option-2 in Fig. 10. Option-2 results in more changes in accumulation rate (if magnetochron thickness in the GPTS is a proxy for time) in the Otter Sandstone Fm than option-1. Also, option-2 gives two additional reverse magnetozones in BS7n.1n, BS7r which are not represented in MT11n. However, magnetochron MT11n is only partially represented in the Belvedere and Aghia Triada sections, with both displaying a tentative reverse submagnetozone near the base (Maron et al. 2019), so MT11n may contain more reverse subchrons than shown in these reference sections. The loss of time at potential hiatuses in the Otter Sandstone at the base of the Chiselbury and Pennington members appears to be small, although perhaps all three correlation options suggest part of MT8r (SC2r in GPTS-A) may be missing, based on the thinner reverse polarity of BS6r.

The statistical evaluation of these correlations shows that correlations to GPT-A (Option-1) gives the better and larger SMI (0.53), but the correlations to GPTS-B give the larger PSI value (Table 3). As a comparison the GPTS-A to GPTS-B statistics show a higher level of similarity, as would be expected, because both are constructed from mostly similar datasets. The median Euclidean distance is smaller (0.48) for the correlation to GPTS-B, suggesting this has some advantage over the correlations with GTS-A. All three correlation options pass the RV-test of similarity at >99% probability (P_{RV} <0.01; Table 3). The more problematic magnetozones (i.e., with larger d_i) for comparison are Anisian magnetochrons MT4r and MT5n using GPTS-B, and BS3r.2r, BS5r, BS6n.1n for GPTS-A (flagged in Fig. 10). All correlation options indicate magnetochrons MT12n and MT11 have larger d_i indicating these are more problematic comparisons.

Comparison to the Triassic of the Central European Basin (CEB)

In the CEB the Longobardian to early Carnian interval are assigned to the Grabfeld Fm (Bachmann and Kozur 2004; Nitsch et al. 2005; Hagdorn and Nitsch 2009), largely based on miospore correlations (Kürschner and Herngreen 2010). Regionally the Grabfeld Fm is divided into three units (lower, middle, and upper) with boundaries locally expressed as disconformities (Nitsch, et al. 2005), but in the Morsleben 52a core as correlative conformities. Sulphate bearing units largely occur in the Lower and Middle Grabfeld Fm, like those seen in the Hook Ebb Mudstone and Little Weston Mudstone members (Fig. 11). A magnetostratigraphy through the Grabfeld Fm in core Morsleben 52a and associated northern CEB cores (Fig. 11), allowed construction of a composite for this formation (Zhang et al. 2020), which has a connected cycle-stratigraphy (Barnasch 2010). The magnetostratigraphy from the Lower and Middle Grabfeld Fm and upper part of the underlying Urfurt Fm shows a fair correspondence to the upper part of the SMF (Fig. 11). This suggests the maximum regressive surface in the Salcombe Mouth Mb may relate to the upper-most regressive interval in the Erfurt Fm, below the flooding surface expressed by the transgressive, marine Grenzdolomit horizon. This correlation is emphasised by the sulphate bearing interval between SS2r to basal SS3n and the dominance of coeval evaporites, typical (Nitsch et al. 2005) of the Middle Grabfeld Fm (Fig. 11). Possible hiatuses may be at the base of the Salcombe Mouth Mb and the base of magnetozone SS2n where there is coincidence of polarity boundaries and beds with distinctly differing lithology to underlying units. In the CEB the Urfurt Fm, unlike the overlying Grabfeld Fm contains sandstone beds, a simple comparison which also applies to the Salcombe Mouth Mb and the overlying Hook Ebb Mudstone pair of units. Therefore, as an approximation the interval from the base of the Pennington Point Mb to the base of magnetozone SS2n is coeval with the mid and upper parts of the Urfurt Fm (Figs. 10, 11), which has a strongly diachronous boundary with the underlying Muschelkalk (Franz. et al 2013)

Correlation of the MMG polarity data to the GPTS is ambiguous around the base of the Carnian. Firstly, miospores place the base of the Carnian below the productive samples in the Little Weston Mudstone Mb (Baranyi et al. 2019), and near the base of the Upper Grabfeld Fm in the CEB (Bachmann and Kozur 2004; Kürschner and Herngreen 2010). Secondly, uncertainty about the GPTS construction in the early Carnian (Julian-1 interval) also leads to duplicate options for correlations of magnetozones SS3n and MK2n (Fig. 11). The most likely correlation for the bases of SS3n and MK2n is with the base of UT1n in both

GPTS-A and GPTS-B (Fig. 11). If the single specimen of conodont *Paragondolella polygnathiformis* (conodont proxy for the base of the Carnian; Rigo et al. 2018) found in the Carnian GSSP at Stuores is representative of its first appearance, then UT1n and UT2n may be duplicates in GPTS-B, and instead magnetochron MA5 (in GPTS-A) may be representative of this interval (Fig. 11). This would suggest SS2r and MK1r are the likely equivalents of MT13r (and MA4r), a magnetochron which so far only has a thickness/duration estimate from the Mayerling section (Gallet et al. 1998).

The upper part of magnetozone SS3n in the Little Weston Mudstone Mb has insufficiently detailed sampling to properly define a polarity stratigraphy. However, by comparison to the upper part of the Grabfeld Fm, it is clear this interval is either condensed, or contains a hiatus. The most likely candidates for either of these scenarios are the palaeosol at 179 m or its underlying halite collapse breccia (Fig. 11). If a hiatus, this may be coeval with a disconformity often inferred at the base of the Upper Grabfeld Fm (Bachmann and Kozur 2004; Hagdorn and Nitsch 2009; Kozur and Weems 2010).

Age of the Dunscombe Mudstone Formation (DMF) and international comparisons

Independent evidence of the age of the DMF are firstly provided using miospores from the Strangman's Cove section, in which Baranyi et al. (2019) placed the Julian-Tuvalian boundary around the upper boundary of the DMF. Their miospore data from the body of the DMF suggest that most of this formation is late Julian (or Julian) in age. Warrington (1971) similar concluded that palynomorph assemblages from the DMF were Carnian in age, and Fisher (in Jeans, 1978) recognised older and younger Carnian palynomorph assemblages with the boundary between them placed within the Lincombe Sandstone Mb. Warrington (1997) also inferred a Carnian-age in two samples from the Lyme Regis Borehole, which probably come from the DMF (Gallois 2006). However, the precision with which the Julian and Tuvalian substages can be identified with miospores in the MMG is uncertain, because as noted by Baranyi et al. (2019), miospore occurrences are often diachronous between the Triassic Germanic and Tethyan realms, and independent age control is poor for miospores from the inferred Tuvalian and Norian of the Germanic realm (Kürschner and Herngreen 2010). Characterising the Carnian-Norian transition using miospore assemblages more generally is also problematic (Cirilli 2010; Lucas et al. 2012; Hounslow et al. 2021b).

Secondly, a single specimen of the spinicaudatan, *Laxitextella multireticulata* (Reible) was found in the Lincombe Sandstone Mb from fallen blocks at Weston Mouth (Kozur in

Gallois 2019). This species also occurs in the Middle and Upper Grabfeld Fm of the CEB (Geyer & Kelber, 2018), and from the Upper Meride Limestone of the southern Alps (Kozur & Weems, 2010). The Upper Meride limestone is early Longobardian in age (Stocker et al. 2012), currently providing the best age calibration of *L. multireticulata* . However, the range of *L. multireticulata* is unknown in detail, and more 'advanced forms' have been described, similar to the younger *L. laxitexta*, which is known to range into the Norian (Geyer & Kelber, 2018). Until more is known about the age range of *L. multireticulata* a single specimen from the DMF cannot be confidently used to infer precise ages.

Thirdly, age can be inferred using negative carbon-isotope excursions (CIE) found in the DMF both in the Strangman's Cove section and the Wiscombe Park boreholes (Miller et al. 2017; Baranyi et al. 2019; marked on Hook Ebb-Strangman's Cove section in Fig. 12 as DIE#). These provide additional means of correlation to marine sections with better age control. The Carnian possesses several CIE in the Julian which are in part well calibrated to biostratigraphy (Mueller et al. 2016; Dal Corso et al. 2018; Lu et al. 2021; Mazaheri-Johari et al. 2021; Li et al. 2022). These are marked on the Ogg et al. (2020), GPTS-A in Fig. 12 (as J1 to J4); although these are less well-calibrated to magnetostratigraphy. CIE also occur in the Tuvalian and basal Lacian interval (Jin et al. 2019; Hounslow et al. 2022a; marked on the GPTS-B column (T1 to L1) in Fig. 12) and are better calibrated to magnetostratigraphy.

The magnetostratigraphy from the late Tuvalian and Julian is generally well characterised by section-based studies from Turkey, Italy, Austria, Slovakia and China (Hounslow and Muttoni 2010; Maron et al. 2019; Figs 11, 12). However, the magnetostratigraphy of the early Tuvalian (Tuvalian-1; Fig. 12) is less certain, and one option is to project the poorly-dated Stockton Formation dataset (Newark Supergroup, E-numbered magnetozones) into the mid Carnian (Figs. 12, 14). This option is used in GPTS-A (Fig. 12) and by Zhang et al. (2020), based on magnetostratigraphy from the northern CEB cores. However, Hounslow et al. (2022a) have proposed a rather different polarity scale for the Tuvalian (GPTS-B; Fig. 12), based partly on polarity datasets from Svalbard and constrained by CIE correlations in the Tuvalian.

In terms of geomagnetic polarity, the most distinctive feature of the Lacian Substage is the dominance of reverse polarity (Newark magnetozones E8r-E12r; chrons UT13r-UT16r; Fig. 14). This clearly associates the dominant reverse polarity in the top of the DMF and lower Littlecombe Shoot Mb (SS7 to SS8r) to the Lacian (Figs. 12, 15). This correlation places the base of the Norian within SS6r.1n or SS7n in the upper part of the DMF (Fig. 12).

520 This part likely has missing intervals at the halite collapse breccias in the section (breccias in
521 SS6-SS7 magnetozones). The preferred correlations shown in Fig. 12 (magnetozones SS5r
522 and SS6n to GPTS-B) are based on the correlation of the DMF isotope excursions DIE4,
523 DIE5 to CIE (T5+T6) and T4 respectively (Fig. 12). Magnetozones SS5n and SS6n may
524 additionally correspond with magnetozones MK5n.1n and MK5n.2n in the Weser Fm from
525 the northern CEB cores (upper red correlation lines in Fig.12).
526 The Little Weston Mudstone Mb and basal DMF are normal-polarity dominated and
527 hence the Julian-1 magnetochron interval UT1n- UT2n in GPTS-A, may correlate with the
528 pattern of polarity changes inadequately represented by the sampling in this part of the MMG
529 (Fig. 12). Overlying chron UT2n (blue labels on GPTS-A) is a reverse polarity dominated
530 interval (MK3r-MK4r at Morsleben; SS3r-SS4r in the DMF), which is probably equivalent to
531 the UT6r - UT9r interval in the GPTS-B (based on data from Svalbard and the Pignola-2
532 section; Maron et al. 2017; Hounslow et al. 2022a). In the DMF the isotope excursion DIE-3
533 likely correlates to the J3+J4 excursions (Mazaheri-Johari et al. 2021) of Julian-2 age (black
534 correlation line in Fig. 12). Based on the association of normal polarity around DIE-1, and the
535 dominantly reverse polarity in UT3r-UT4r, it seems less likely that DIE-2 is the equivalent of
536 excursion J2 known from the earliest Julian-2 (Fig. 12). A better alternative is that a missing
537 interval may be present at the halite collapse breccia in SS3r, and DIE-2 and DIE-1 are
538 probably older CIEs within Julian-1 (e.g., as in Mueller et al. 2016). This suggests the reverse
539 polarity of the Lincombe Sandstone Mb is coeval with that of the Stuttgart Fm in the
540 Morsleben cores, and both are early Tuvalian in age. Since the polarity changes across the
541 base of the Lincombe Sandstone Mb, this level could be a minor hiatus/missing interval (Fig.
542 13) because this sandstone has a channel-like (but not clearly down-cutting) geometry (Porter
543 and Gallois 2008).
544 A magnetostratigraphy from the Polish 'Schilfsandstein' (Nawrocki et al. 2015,
545 Wójcik et al. 2017) has indicated three normal polarity submagnetozones, in a dominantly
546 reverse polarity interval like the style of polarity changes in the Stuttgart Fm of the
547 Morsleben cores; although in Poland fragmentary recovery of polarity from over and
548 underlying strata precludes any detailed correlation. Refinement of the association of carbon
549 isotope excursions with respect to the magnetostratigraphy in the late Julian would assist with
550 international correlation at a finer scale.
551 The statistical assessment of these correlations shows that SMI is largest for the DMF
552 to Morsleben correlations, with the largest PSI for the DMF to GPTS-B correlations (Table

553 3). This later correlation also has the smallest median d_i (at 0.77), and the larger probability of
554 association (more than 99% chance of association). This suggests statistically the correlation
555 to GTPS-B is the better, with the most problematic intervals for comparison being SS4r,
556 SS6n and SS6r.1r (Fig. 12). For comparison, the GPTS-A to GPTS-B correlations have
557 smaller SMI and PSI indices, indicating poorer relationships. This is probably because these
558 are constructed from entirely different polarity datasets through the Tuvalian.

559 *Comparison to the Stuttgart and Weser formations of the CEB*

560 At a simple-level, the sandstone and calcareous 'group' divisions of Jeans (1978) for
561 the DMF (Fig. 13) are like the halite-sandstone-halite bearing 'sandwich' of the Stuttgart Fm
562 and its adjacent formations in the CEB (Bachmann et al. 2010; Hagdorn and Nitsch 2009).
563 The presence of dolostone beds in both successions also enhances the degree of similarity to
564 the DMF, with flooding surfaces in the CEB usually represented by dolostone beds. Using the
565 magnetostratigraphic correlations and the events and cycles of Barnsach (2010) from the
566 Morsleben 52a core, and Franz et al. (2014) from more widely in the CEB, some of these
567 flooding surfaces may have coeval expression in the Devon successions; particularly those of
568 the Neubrandenburg, Beaumont and Lehrberg beds (Figs. 12, 13). However, the small cycles
569 of Barnsach (2010) do not have a clear synchronous expression in the DMF.
570 The set of halite-dissolution breccias in the Upper Weser Fm from the Moresleben
571 52a core, and those near beds K and J in the DMF may be indicative of coeval flooding
572 events around the base of the contemporary SS7r and MK5r.1r magnetozones (Fig. 13).
573 Indeed, three widely distributed halite units are known in the CEB in the Weser Fm
574 (Bachmann et al. 2010), which may be coeval with the three collapse breccias seen in the
575 upper part of the DMF between 26- 30 m (Fig. 13). If these relationships are correct, the
576 boundary between the Weser and Arnstadt formations (the D4 or early Kimmerian-I
577 unconformity; Feist-Burkhardt et al. 2008) may be coeval with the sequence boundary at bed
578 N in the base of the Littlecombe Shoot Mudstone Mb (Fig. 13).
579 Despite episodic eustatic marine influence on the Middle Keuper in the CEB (sourced
580 through a southern gateway; Bachmann et al. 2010; Franz et al. 2014), and the correlations
581 proposed in Fig. 13, there is no direct evidence for marine intervals in the Wessex Basin in
582 this interval. If there was, this would likely be a route from the SW through the SW
583 Approaches basins (McKie 2017). More detailed investigation of the dolostone intervals in
584 the DMF may shed light on this possibility.

585 ***Rhaetian and upper Norian: Blue Anchor Formation (BAF), Seaton and Haven***
586 ***Cliff Mudstone members***

587 In addition to the miospore data discussed above in the base of the Branscombe
588 Mudstone Fm, palynomorphs from the upper parts of the BAF suggest a Rhaetian age
589 (Warrington 1997, 2005). These Rhaetian assemblages are comparable to those from the St
590 Audrie's Bay section in North Somerset, where similar assemblages continue into the Penarth
591 Group (Hounslow et al. 2004; Bonis et al. 2010).

592 Alternative GPTS's have been proposed for the mid Norian to early Rhaetian. Firstly,
593 that of Kent et al. (2017) and Maron et al. (2019) utilise a reference scale largely from the
594 Newark Supergroup magnetostratigraphy (Fig. 15), with the chronostratigraphy imported
595 using a correlation to selected marine sections with magnetostratigraphy. Secondly, is the
596 GPTS-B (Fig. 14) a marine-section based composite of Hounslow and Muttoni (2010), which
597 is updated here with new data for the Sevatian to early Rhaetian (see SI Fig. S5.1).
598 Correlations between GPTS-B and some key non-marine sections for this interval are shown
599 in Fig. 14, with the addition of a composite for the upper Chinle Formation (its construction
600 is outlined in SI section 5.1). GTPS-B provides the better base to understand the likely
601 chronostratigraphy of the upper parts of the MMG (Fig. 15).

602 The magnetostratigraphy from the Haven Cliff section is closely comparable to that
603 from the St Audrie's Bay section (Fig. 15), even down to the reverse submagnetozones in the
604 coeval mid parts of HC2n and SA4n and the probably coeval reverse submagnetozones
605 SA3n.1r and HC1n.1r (Fig. 15). The relative thicknesses of coeval magnetozones varies
606 somewhat between these sections, but both are closely comparable to the
607 magnetostratigraphy from the upper Passaic Fm (E16n to E19 magnetozones) of the Newark
608 Supergroup (Fig. 15). These relationships are also consistent with an unanchored
609 astrochronology from the MMG at St Audrie's Bay and its synchronisation with the Newark
610 Supergroup cyclostratigraphy (Kemp & Coe, 2007). Newark magnetozones E15 to E19 are
611 widely associated with late Norian (Sevatian age strata) and their transition into the earliest
612 parts of the Rhaetian (Fig. 14; SI Figs. S5.1, S5.2; Maron et al. 2019). Based on these
613 magnetostratigraphic correlations, the two proposed choices for the base of the Rhaetian
614 (NRB1 and NRB2 in Figs. 14, 15), place the Rhaetian boundary either in the upper part of the
615 Haven Cliff Mudstone, or within the lowest part of the BAF (Fig. 15). This indicates that
616 magnetozone HC1n (in the Haven Cliff section) should equate to Newark magnetozone
617 E16n, St Audrie's Bay magnetozone SA3n and magnetochron UT22n.

The age of NRB1 based on the anchored astrochronology from Austrian sections places it at ~208 Ma (Galbrun et al. 2020), consistent with both the placement of NRB1 (from magnetostratigraphic correlations in Fig. 14) and the anchored astrochronological age (207.6 Ma; Kent et al. 2017) for the base of E18r in the Newark Supergroup (Fig. 14). Based on the biostratigraphy from the Chinle Fm; the Redonda Mb (magnetozone CC8n-CC10n interval; Fig. 14) is usually assigned a Rhaetian age (Zeigler and Geissmann 2011; Heckert and Lucas 2015). In addition, the similarity in Chinle Fm detrital zircon ages to the Newark-Hartford APTS ages between CC5r-CC9n (E14r- E18n in Newark-Hartford APTS) indicates a close correspondence between the polarity patterns in the Chinle Fm and Newark Supergroup (top left Fig. 15), and the corresponding interval in GPTS-B. This locates NRB1 near the base of magnetozone CC9r in the Chinle Fm composite, and consequently robustly demonstrates the international consistency in the polarity patterns in this Sevatian to early Rhaetian interval, from magnetochrons UT20r to UT24r (Fig. 14).

In the Wessex Basin the interval encompassing the Seaton Mudstone Mb to the base of the BAF is regionally rather consistent in thickness (Gallois 2001; 2003), with the nearest borehole to the coastal outcrops (at Marshwood) showing ~ 145 m (Gallois 2003) for this interval. This is used as a thickness estimate for the Seaton Mudstone Mb in the coastal outcrops. We consider that magnetozone SS12n is not the equivalent of either HC1n, SS11n or SS10n, also in the Seaton Mudstone Mb, for the following reasons. Firstly, projecting the top of the Seaton section (above the sampled interval), based on a test of the equivalence of SS12n and HC1n, would indicate that the Haven Cliff Mudstone Mb should be close to the top of the Seaton section; yet there is no evidence of the Haven Cliff Mudstone Mb in the Seaton fault blocks. Secondly, the mudstones from the Seaton Mudstone Mb in the Branscombe section, have cm-scale sandy laminae which are absent from the Seaton Cliff section, suggesting these sections are not lithologically equivalent. Thirdly, SS11n is some 23 m thick compared to 14 m for SS12n and also have no consistent lithological matches using the detailed logs (see the SI). Fourthly, SS10n (11 m thick) is a similar thickness to SS12n, yet any lithological match, using the assumption of magnetozone equivalence is poor. Also, this match would require the Red Rock Gypsum Mb to be shortly below the Seaton section, a situation for which there is no evidence in the ~40 m of poorly exposed outcrop to the west in the Axe valley fault blocks. The later three arguments suggest that magnetozone SS12n is not equivalent to magnetozones SS11n or SS10n seen in the Branscombe Mouth section. Using the above thickness estimate of the Seaton Mudstone Mb and the cumulative sampled

651 thicknesses of this member, indicates that ~26 m of this member remains unsampled from
652 this study.
653 Therefore, magnetozone SS12n is inferred to be magnetochron UT21n, as also seen in
654 the basal part of the St Audrie's Bay section (SA2n; Fig. 15 and E15n in the Newark APTS).
655 Additional support for this is that the pattern of polarity changes in the Seaton Cliff section is
656 like that in magnetozone CC6n in the Chinle Fm. Also, both the Pizzo Mondello and Kavur
657 Tepe sections have reverse sub-magnetozones in UT21n, like those detected within CC6n and
658 SS12n, similarities strengthening this proposed correlation.

659 *The Branscombe Mudstone Formation and the middle Norian (Alaunian)*

660 The interval from magnetozones SS9n to SS11n contains three major normal polarity
661 intervals (SS9n, SS10n, SS11n), like both the marine-based GPTS-B, and the interval CC4n
662 to CC5n in the upper Chinle Fm composite (Fig. 15). For this reason, and the constraints
663 from overlying and underlying polarity patterns, we correlate the interval SS9n - SS11n with
664 UT18n - UT20n (Fig. 16). However, this interval is unlike the Newark Supergroup APTS,
665 which has only two thick normal magnetozones over this interval. This suggests that the
666 Newark Supergroup magnetozone interval E14n-E14r may be incomplete (marked in Fig.
667 15). Other than the marine-based sections over this interval, there are also coeval non-marine
668 sections from the Fleming Fjord Group and the Los Colorados Fm (Fig. 14). The middle
669 Norian interval has also been evaluated in cores and sections from the Holy Cross Mountains
670 in Poland (Wojcik et al. 2017) through the Arnstadt Formation, which displays a pattern of
671 polarity reversals similar in overall style to the UT18n to UT21n, although the fragmentary
672 recovery of polarity precludes a detailed comparison.
673 The magnetostratigraphy from the Fleming Fjord Group does not extend to older
674 strata to confirm the polarity pattern UT18n-UT20n, but matches well with GTPS-B (Fig.
675 14), using the preferred correlation of Kent and Clemmenson (2021) and the coeval parts of
676 the Newark APTS. Some 60 m below the base of the Colorados Fm is a precise ID-TIMS
677 zircon date (i.e., 221.8 ±0.3 Ma), which when compared to the Chinle Fm composite (with its
678 detrital zircon dates), suggests the magnetostratigraphic match shown as Option-2 in Fig. 14.
679 The correlation shown as Option-1 was that preferred by Kent et al. (2014) based on the less
680 precise Ar/Ar date (225.9 ±3.7 Ma), which also gives a satisfactory polarity match between
681 the upper part of the Colorados Fm and magnetochrons UT18n to UT20n (Fig. 14), but
682 unsatisfactory match using the more precise ID-TIMS date.

The proposed missing interval in the Newark APTS (marked in Figs. 14, 15) corresponds with an abrupt upwards decrease in accumulation rate near the boundary of magnetozones E14n-E14r (from ~24 to 14 cm/ka), based on the astrochronology using depth rank and colour (Meyers 2019; Wang et al. 2022). This suggests an abrupt and major shift in sedimentary regimes at the proposed position of the missing interval.

These strands of evidence, along with the new data from the MMG, although not conclusive by themselves, collectively support the Newark APTS to GPTS-B correlation shown in Figs. 14, 15. Significantly this solution may solve the long-running debate (Gallet et al. 2003; Muttoni et al. 2004; Hounslow and Muttoni 2010; Galbrun et al. 2020; Ogg et al. 2020) about how the Newark APTS in the mid Norian relates to the marine-based GPTS. This conundrum is fundamentally linked to ambiguity in how to relate the biostratigraphy of the Newark Supergroup to international stages (Tanner and Lucas 2015; Galbrun et al. 2020). With the solution proposed here, the chronostratigraphic and biostratigraphic divisions of the Norian are now satisfactorily aligned with the astrochronology from the Newark Supergroup (Fig. 14). This interpretation indicates the Branscombe Mudstone Fm contains the full complement of magnetochrons known from the early Norian to the early Rhaetian (Fig. 15).

The statistical evaluation of these correlations shows that the GPTS-B to Chinle composite show the strongest association with the largest SMI, PSI and smallest median d_i (Table 3). The Newark Supergroup APTS to Chinle composite shows a similar level of association as between the GPTS-B and the MMG, with all three of these having a probability of association > 99% (P_{RV} <0.01; Table 3). Magnetozones SS9n.2n, SS9r.3r, HC2n.2n and HC2r, have the larger d_i indicating more divergence of these zones. These statistics support the overall correlation relationships proposed above. They also suggest that in spite of the very different tectonic and sedimentologic settings of these three terrestrial successions, they all share a common record of polarity changes which is not impacted to a major extent by hiatus. This does not mean that these successions are complete, as inferred at the hiatuses in the MMG, it may just indicate that at the time-scale of polarity changes, the sediment record is sufficiently complete to approximate the relative length-scales of most major magnetochrons.

Controls on accumulation rates in the Mid-Late Triassic in Britain

With the proposed correlation to the polarity scales, we estimate accumulation rates in the Otter Sandstone Fm and Mercia Mudstone Group. Attachment of polarity boundaries to

chronometric time used the Bayesian age model of Hounslow et al. (2018) for the Middle Triassic to early Carnian (polarity chrons up to UT5n). The late Carnian to Rhaetian interval used the Newark Supergroup astrochronology of Kent et al. (2017) and Wang et al. (2022), which give only slightly different ages for the magnetochrons. That using the Bayesian age model and Kent et al. (2017) ages is referred to as age model-1 and that using the Bayesian age model and Wang et al. (2022) ages is model-2 (Fig. 16). As an alternative to the late Ladinian-Carnian part of these models we also use the chronometric scale proposed by Zhang et al. (2020). Alternatively, Miller et al. (2017) proposed a 1.09 Myr duration (based on an astrochronology from the Wiscombe Park borehole) for the interval from the base of the DMF to near the correlated base of magnetozone SS6r. This same interval gives a duration of 7.0 Myr and 8.1 Myr using age model-1 and the Zhang et al. (2020) age model respectively. Likely the ca 8 m cycles identified by Miller et al. (2017) are closer to 2.4 Myr eccentricity cycles.

Using these three age models, instantaneous accumulation rates between polarity boundary ages were estimated (data points in Fig. 16). The accumulation rates are not significantly impacted by the inferred missing interval in the Newark Supergroup APTS, because rates are based on chron durations. Since the age estimates of polarity boundaries in the MMG are likely biased by sampling resolution and fidelity of polarity recovery, and by uncertainties in the chronometric estimation of magnetochrons in the age models, we have averaged the accumulation rates (using a 3-point geometric mean) for the model-1 and Carnian age models (Fig. 16). The alternate Carnian age model does not significantly modify the accumulation rates. These accumulation rates also include the potential missing time at the likely hiatus levels identified.

These data indicate thye Devon coastal succession overall has a baseline accumulation rate of 30-50 m/Myr throughout this interval, which presumably relates to typical subsidence and accommodation space availability in this part of the Wessex Basin. There are several deviations from the baseline rates (Fig. 16).

In the upper part of the Otterton Ledge Mb there is a reduction of accumulation rate to ~10-20 m/Myr, which corresponds with the upper part of the 2nd fluvial cycle of Newell (2018a) in this member. This reduction in accumulation rate corresponds with the Anisian-Ladinian boundary interval. In the northern part of the CEB the Illyrian-Fassanian boundary also corresponds with the initial regression of the Lower Keuper (Erfurt Fm) over the marine limestones of the Upper Muschelkalk. In the southern CEB, with a stronger marine influence,

748 this diachronous regression was completed in the late Fassanian (Franz et al. 2013). The
749 facies shift expressed by Muschelkalk-Keuper transition is the major environmental change
750 of the Middle and Upper Triassic Germanic facies in Europe. Our dating shows that the Otter
751 Sandstone-MMG transition (Chiselbury to Sid Mudstone members) is coeval with this
752 diachronous environmental shift. However, the Wessex Basin was not hydrologically
753 connected to the CEB (McKie 2014) in this interval. More importantly in the Wessex Basin
754 this transition shows a transgressive relationship. The transgressive character is shown most
755 clearly above the sequence boundary (Gallois 2005; Newell 2018a) at the base of the
756 Pennington Point Mb, which is an erosive transgressive surface with an overlying
757 transgressive system tract (TST) extending into the Salcombe Hill Mudstone Mb (Fig. 16).
758 The nature and boundaries of the Pennington Point Mb indicate it genetically belongs to the
759 MMG successions (Gallois 2003). Although the CEB and the Wessex Basin have opposite
760 sequence stratigraphic tracts in this age interval, they both show a flood of silt-and clay-grade
761 siliclastics overwhelming carbonate and fluvial sand-prone systems respectively. In the CEB
762 the source of sand was predominantly from Scandinavia in the Keuper (Paul et al. 2008), but
763 from Cadomian basement rocks of the Armorican Massif throughout the Otter Sandstone Fm
764 (Morton et al. 2013). The likely common factor linking the incoming Erfurt Fm and MMG
765 successions was an increasing aridification and greater supply of loessic silt and clay during
766 the transition into the Ladinian. Loessic silt may have had a bigger impact on the dry-playas
767 (McKie 2017), of the Sidmouth Mudstone Fm, than in the CEB, where wet-playa facies tend
768 to dominate in coeval mudstones (Aigner and Bachmann, 1989; McKie 2017).
769 The DMF shows the largest reduction in accumulation rates, which began in the upper
770 part of the Little Weston Mudstone Mb and shows recovery through the lower part of the
771 Littlecombe Shoot Mudstone Mb (Fig. 16). This dramatic reduction in accumulation rates is
772 likely associated with Carnian environmental changes that are best understood in the mid-
773 Carnian (Dal Corso et al. 2020). Probable causes of this large reduction in accumulation rate
774 are:
775 A. **Fine-sediment bypass**: the sink for detrital fines was largely directed to basin
776 depocenters with sand- grade material remaining at basin margins and within channel
777 systems that are directed to basin depocenters (Porter & Gallois 2008). Certainly,
778 during the Carnian much greater thicknesses of halite accumulated in depocenters in
779 the Wessex Basin (Gallois 2003), probably coeval with the halite-breccia intervals
780 above and below the sand-bearing interval in the DMF. The basin-flank halite

deposits were likely re-worked during ephemeral periods of high groundwater and re-charged to depocenters (McKie 2017), as inferred in the CEB by Franz et al. (2014). A similar style of Carnian-age, by-pass basin-filling is seen in the CEB, giving distinctive depocenter sags from filling of accommodation space, particularly during the interval of the Grabfeld Fm (Bachmann et al. 2010). Alternatively, this geometry is commonly inferred as a pulse of renewed extensional tectonics (Bachman et al. 2010; McKie 2017), rather than flank condensation with sediment by-pass and accommodation spacing filling. Rejuvenated extensional subsidence does not concur with the observed reduction in basin flank accumulation rates.

B. **Shut down in fine sediment supply** from hinterlands and desert margins: This comes about by lack of supply, perhaps caused by enhanced vegetation trapping in hinterland soils or lakes, so that loessic sources areas ceased to supply the same volume of fines, yet the limited supply of fluvial-derived sand+fines continued. At the present-day, desert dusts in low latitudes are principally supplied from desert margins, with the largest single sources being from deflation of lake basins (Bristow et al. 2009), providing seasonally phased supplies of dust (Middleton 2017; Li et al. 2020).

The conundrum of the mid Carnian in western European Germanic-style basins is the sedimentological indication of sandy, wetter lacustrine and fluvial systems in the mid Carnian (Porter and Gallois 2008; Kozur and Bachmann 2010; Franz et al. 2019; Ruffell et al. 2015), yet palynological data suggest similar dry-land vegetation (xerophytes) throughout the Carnian crisis (Baranyi et al. 2019; Franz et al. 2019). One way to balance this apparent dichotomy is a flashier riverine input, so that ephemeral/seasonal storms deliver the sand-grade material, yet ground water and soil moisture is not maintained throughout the growing season, so hygrophytic flora was not able to fully develop, a situation which has been proposed for the Carnian of the Wessex Basin (Baryani et al. 2019). A greater contribution from xerophytic regionally-derived pollen rain, may also have limited the ability to detect local hygrophytic vegetation that developed during these brief wetter intervals. This imbalance may have been enhanced by spread of hinterland xerophytes, into previously hyper-arid areas, due to seasonally more humid, but annually essentially dry desert margins. This may be linked to point B above. Franz et al. (2014) have proposed an alternative scenario for the Stuttgart Fm in the CEB invoking marine transgressions as the forcing factor for local development of hygrophytes, which is not applicable in the Wessex Basin due to a lack of evidence for marine influence.

The dry playa facies of the Branscombe Mudstone Fm do not reach maximum accumulation rates until the mid Norian, at around the position of the Red Rock Gypsum Mb, which likely represents an interval of wet-playa facies (i.e., facies divisions of McKie 2017), probably marking a maximum flooding surface. A second maximum flooding surface in the late Alaunian corresponds with a distinctive high gamma pick seen consistently on log profiles in the Wessex Basin (Gallois 2003; Newell 2018b). This likely relates to an interval with cm-thick black mudstones which are exposed on the low tide beach below the Seaton section (so likely in magnetozone UT20r; Fig. 15). This 'high gamma event' heralds a decline into lower accumulation rates in the upper Seaton Mudstone Mb, and the development of wet-playa facies in the Haven Cliff Mudstone Mb and BAF. Since the units above the Red Rock Gypsum Mb are consistent in thickness across the Wessex Basin (Gallois 2003), the likely reason for the accumulation rate decrease may be increasing humidity into the Sevatian and early Rhaetian, impacting sediment supply, like outlined in B) above.

Conclusions

1. A magnetostratigraphy is recovered from most of the 474 m of the Mercia Mudstone Group from coastal outcrops in the type-section of the group. Some outcropping intervals need refining, because the sampling density is inadequate to robustly define some thin magnetozones.
2. Characteristic magnetisations are largely carried by haematite, but with some rare levels in the Dunscombe Mudstone Fm where magnetisations are carried by magnetite.
3. The magnetostratigraphy can be correlated with better dated marine and non-marine sections elsewhere, and thus establishes the first accurate chronostratigraphy for the MMG. The interval studied ranges from the early Ladinian (mid Fassanian Substage) to the early part of the Rhaetian. Other geochronological tools applied to the MMG, such as cyclostratigraphy, may assist in improving and adapting the proposed age assignments.
4. Using our data and a collective assessment of magnetostratigraphies from other Norian sections, allows us to proposal a solution to the long-standing debate about the polarity pattern through the mid Norian.
5. The interval of the Hook Ebb Mudstone to Little Weston Mudstone members is closely comparable in facies and age to the Grabfeld Fm in the CEB.
6. A comparison of our magnetostratigraphy to that from the Middle Keuper Group of the CEB indicates a close similarity to the Dunscombe Mudstone Fm, including the

equivalence of sandstone-bearing intervals of the Lincombe Sandstone Mb and the Stuttgart Fm of the CEB. The coeval nature of some flooding surfaces and the timing of evaporites between the Dunscombe Mudstone Fm and the Weser Fm of the CEB indicates synchroneity of some climatic events between these two basins. Additional work on the more sparsely-sampled upper part of the Little Weston Mudstone Mb would improve the chronology of this apparent Julian age interval.

7. Using the derived age models of the Devon succession, accumulation rates are dramatically lower from the mid Carnian, but show recovery in the early Norian. These changes reflect sediment by-pass on the flanks of the Wessex Basin and a major slowdown in fine sediment delivery. This was likely due to limited aeolian supply of dust from shrinkage of the hyper-arid source areas, caused by seasonal climatic humidification from the mid Carnian to earliest Norian.
8. The data detailed here enables environments and habitats in the Middle-Late Triassic in Britain to be better related to other widely geographically spaced localities and it should improve details of palaeogeological maps, bringing the British Triassic succession into much better time-alignment with the Germanic Triassic.

Acknowledgements Magnetic measurements were also performed by Guy Jenkins, Paulette Posen and Vassil Karloukovski. Guy Jenkins, Paulette Posen and Julian Andrews assisted with early fieldwork. Neil Jones kindly supplied MWH with logs of some of these sections during initial field work. We thank Geoff Warrington and Richard Edwards who aided preliminary investigations, and Rob Coram for stratigraphical advice. The reviewers Spencer Lucas, John Geissman and the Editor provided constructive comments on drafts that led to improvements in the present account.

Funding BGS grant GA/98E/31/A1 initiated this work. Part of the fieldwork and measurements on the Seaton section was funded by a NERC grant to Gordon Walkden with some additional fieldwork support from Wolfram Kürschner. Part of the work at Haven Cliff was funded by Leverhulme Trust grant F/204/W.

875 ## References

876 Aigner, T. and Bachmann, G.H. 1989. Dynamic stratigraphy of an evaporite-to-red bed
877 sequence, Gipskeuper (Triassic), southwest German Basin. *Sedimentary Geology*, 62,
878 5-25.
879 Bachmann, G.H. and Kozur, H.W. 2004. The Germanic Triassic: correlations with the
880 international chronostratigraphic scale, numerical ages and Milankovitch cyclicity.
881 *Hallesches Jahrbuch für Geowissenschaften*, 26, 17-62.
882 Bachmann, G.H., Geluk, M.C., Warrington, G., Becker-Roman, A., Beutler, G., Hagdorn, H.,
883 Hounslow, M.W., Nitsch, E., Rohling, H.G., Simon, T. and Szulc, A. 2010. Triassic.
884 *In:* Doornenbal, H. and Stevenson, A. (eds) *Petroleum geological atlas of the*
885 *Southern Permian Basin area*. EAGE, 149-173.
886 Baranyi, V., Miller, C.S., Ruffell, A., Hounslow, M.W. and Kürschner, W.M. 2019. A
887 continental record of the Carnian Pluvial Episode (CPE) from the Mercia Mudstone
888 Group (UK): palynology and climatic implications. *Journal of the Geological Society*,
889 176, 149-166.
890 Barnasch, J., 2010. *Der Keuper im Westteil des Zentraleuropäischen Beckens (Deutschland,*
891 *Niederlande, England, Dänemark): diskontinuierliche Sedimentation, Litho-, Zyklo-*
892 *und Sequenzstratigraphie.* Schriftenreihe der Deutschen Gesellschaft für
893 Geowissenschaften, 7-169.
894 Benton, M.J. 1997. The Triassic reptiles from Devon, *Proceedings of the Ussher Society*., 9**,**
895 141-152.
896 Benton, M.J., Warrington, G.., Newell, A.J. and Spencer, P.S. 1994. A review of the British
897 Middle Triassic tetrapod assemblages. *In*: Fraser, N.C and Sues, H-D. (eds), *In the*
898 *Shadow of the Dinosaurs*, 131-160. Cambridge University Press, Cambridge.
899 Benton, M.J., Cook, E. and Turner, P. 2002. *Permian and Triassic Red Beds and the Penarth*
900 *Group of Great Britain*. Geological Conservation Review Series, No. 24. Joint Nature
901 Conservation Committee, Peterborough.
902 Bernardi, M., Gianolla, P., Petti, F.M., Mietto, P. and Benton, M.J. 2018. Dinosaur
903 diversification linked with the Carnian Pluvial Episode. *Nature Communications*, 9,
904 1-10.
905 Bonis, N.R., Ruhl, M. and Kürschner, W.M. 2010. Milankovitch-scale palynological turnover
906 across the Triassic–Jurassic transition at St. Audrie's Bay, SW UK. *Journal of the*
907 *Geological Society*, 167, 877-888.

908 Brayard, A., Escarguel, G., Bucher, H., Monnet, C., Brühwiler, T., Goudemand, N., Galfetti,
909 T. and Guex, J. 2009. Good genes and good luck: ammonoid diversity and the end-
910 Permian mass extinction. *Science*, 325, 1118-1121.
911 Bristow, C.S., Drake, N. and Armitage, S. 2009. Deflation in the dustiest place on Earth: the
912 Bodélé Depression, Chad. *Geomorphology*, 105, 50-58.
913 Broglio Loriga, C., Cirilli ,S., De Zanche, V., di Bari, D., Gianolla, P., Laghi, M.F., Lowrie,
914 W., Manfrin, S., Mastandrea, A., Mietto, P., Muttoni, C., Neri, C., Posenato, C.,
915 Rechichi, M.C., Rettori, R., and Roghi, G. 1999, The Prati di Stuores/Stuores Wiesen
916 Section (Dolomites, Italy): a candidate Global Stratotype Section and Point for the
917 base of the Carnian stage. *Rivista Italiana di Paleontologia Stratigraphia,* 105, 37-78.
918 Butler, M. 1998. The geological history and the southern Wessex Basin- a review of new
919 information from oil exploration. In: Underhill, J. R. (ed), *Development, evolution*
920 *and petroleum geology of the Wessex Basin.* Geological Society London Special
921 Publication 133, 67-86.
922 Cirilli, S., 2010. Upper Triassic–lowermost Jurassic palynology and palynostratigraphy: a
923 review. *In:* Lucas, S.G. (ed) *The Triassic timescale*, *Geological Society, London,*
924 *Special Publications*, 334, 285-314.
925 Clegg, J.A., Almond, M. and Stubbs, P.H.S. 1954. LXVI. The remanent magnetism of some
926 sedimentary rocks in Britain. *The London, Edinburgh, and Dublin Philosophical*
927 *Magazine and Journal of Science*, 45, 583-598.
928 Coram, R.A., Radley, J.D. and Benton, M.J. (Anisian) Otter Sandstone biota (Devon, UK):
929 review, recent discoveries and ways ahead. *Proceedings of the Geologists'*
930 *Association*, 130, 294-306.
931 Creer, K.M. 1959. AC demagnetization of unstable Triassic Keuper Marls from SW England.
932 *Geophysical Journal of the Royal Astronomical Society*, 2, 261-275.
933 Creer, K.M. 1961. Superparamagnetism in red sandstones. *Geophysical Journal of the Royal*
934 *Astronomical Society*, 5, 16-28.
935 Creer, K.M., Irving, E. and Runcorn, S.K. 1954. The direction of the geomagnetic field in
936 remote epochs in Great Britain. *Journal of geomagnetism and geoelectricity*, 6, 163-
937 168.
938 Dal Corso, J., Gianolla, P., Rigo, M., Franceschi, M., Roghi, G., Mietto, P., Manfrin, S.,
939 Raucsik, B., Budai, T., Jenkyns, H.C. and Reymond, C.E. 2018. Multiple negative

carbon-isotope excursions during the Carnian Pluvial Episode (Late Triassic). *Earth-Science Reviews,* 185, 732-750.

Dal Corso, J., Bernardi, M., Sun, Y., Song, H., Seyfullah, L.J., Preto, N., Gianolla, P., Ruffell, A., Kustatscher, E., Roghi, G. and Merico, A. 2020. Extinction and dawn of the modern world in the Carnian (Late Triassic). *Science Advances*, 6, page numbers? DOI: 10.1126/sciadv.aba009

Feist-Burkhardt, S., Götz, A.E., Szulc, J., Borkhataria, R., Geluk, M., Haas, J., Hornung, J., Jordan, P., Kempf, O., Michalík, J. and Nawrocki, J. 2008. Triassic. *In:* McCann, T. (ed). *The Geology of Central Europe Volume 2: Mesozoic and Cenozoic*, Geological Society of London, 749-822. https://doi.org/10.1144/CEV2P.1

Franz, M., Henniger, M. and Barnasch, J. 2013. The strong diachronous Muschelkalk/Keuper facies shift in the Central European Basin: implications from the type-section of the Erfurt Formation (Lower Keuper, Triassic) and basin-wide correlations. International *Journal of Earth Sciences*, 102, 761-780.

Franz, M., Nowak, K., Berner, U., Heunisch, C., Bandel, K., Röhling, H.G. and Wolfgramm, M., 2014. Eustatic control on epicontinental basins: the example of the Stuttgart Formation in the Central European Basin (Middle Keuper, Late Triassic). *Global and Planetary Change,* 122, 305-329.

Franz, M., Kustatscher, E., Heunisch, C., Niegel, S. and Röhling, H.G. 2019. The Schilfsandstein and its flora; arguments for a humid mid-Carnian episode?. *Journal of the Geological Society*, 176, 133-148.

Furin, S., Preto, N., Rigo, M., Roghi, G., Gianolla, P., Crowley, J.L. and Bowring, S.A., 2006. High-precision U-Pb zircon age from the Triassic of Italy: Implications for the Triassic time scale and the Carnian origin of calcareous nannoplankton and dinosaurs. *Geology*, 34, 1009-1012.

Galbrun, B., Boulila, S., Krystyn, L., Richoz, S., Gardin, S., Bartolini, A. and Maslo, M., 2020. " Short" or "long" Rhaetian? Astronomical calibration of Austrian key sections. *Global and Planetary Change*, 192, doi.org/10.1016/j.gloplacha.2020.103253

Gallet, Y., Krystyn, L. and Besse, J. 1998. Upper Anisian and lower Carnian magnetostratigraphy from the northern Calcareous Alps (Austria), *Journal of Geophysical Research*, 103, 605-622.

Gallet, Y., Krystyn, L., Besse, J. and Marcoux, J. 2003. Improving the Upper Triassic numerical time scale from cross-correlation between Tethyan marine sections and the

973 continental Newark basin sequence. *Earth and Planetary Science Letters*, 212, 255-
974 261.
975 Gallet, Y., Krystyn, L., Marcoux, J. and Besse, J. 2007. New constraints on the end-Triassic
976 (Upper Norian–Rhaetian) magnetostratigraphy. *Earth and Planetary Science Letters,*
977 255, 458-470.
978 Gallois, R.W. 2001. The lithostratigraphy of the Mercia Mudstone Group (mid and late
979 Triassic) of the south Devon coast. *Geoscience in south-west England* , 10, 195-204.
980 Gallois, R.W. 2003. The distribution of halite (rock salt) in the Mercia Mudstone Group (mid
981 to late Triassic) in south-west England. *Geoscience in south-west England*, 10, 383-
982 389.
983 Gallois, R.W. 2005. The type section of the junction of the Otter Sandstone Formation and
984 the Mercia Mudstone Group (mid Triassic) at Pennington Point, Sidmouth.
985 *Geoscience in south-west England*, 11, 51-58.
986 Gallois, R.W. 2006. Correlation of the Triassic and Jurassic successions proved in the Lyme
987 Regis (1901) borehole with those exposed on the nearby Devon and Dorset coasts.
988 *Geoscience in south-west England*, 11, 99-105.
989 Gallois, R.W. 2007. The stratigraphy of the Mercia Mudstone Group succession (mid to late
990 Triassic) proved in the Wiscombe Park boreholes, Devon. *Geoscience in south-west*
991 *England*, 11, 280-286.
992 Gallois, R.W. 2019. The stratigraphy of the Permo-Triassic rocks of the Dorset and East
993 Devon Coast World Heritage Site, UK. *Proceedings of the Geologists' Association*,
994 130, 274-293.
995 Gallois, R.W. and Porter, R.J. 2006. The stratigraphy and sedimentology of the Dunscombe
996 Mudstone Formation (late Triassic) of south-west England. *Geoscience in south-west*
997 *England*, 11, 174-182.
998 Geyer, G. and Kelber, K.P. 2018. Spinicaudata ("Conchostraca," Crustacea) from the Middle
999 Keuper (Upper Triassic) of the southern Germanic Basin, with a review of Carnian–
1000 Norian taxa and suggested biozones. *PalZ*, 92, 1-34.
1001 Hagdorn, H. and Nitsch, E. 2009. *Field guide to the 6th International Triassic Field*
1002 *Workshop (Pan-European Correlation of the Triassic): Triassic of Southwest*
1003 *Germany*, Institut für Geowissenschaften der Universität Tübingen,72p.
1004 http://www.stratigraphie.de/perm-trias/Triassic_workshop_2009_guide.pdf.

1005 Haque, Z., Geissman, J.W., Irmis, R.B., Olsen, P.E., Lepre, C., Buhedma, H., Mundil, R.,
1006 Parker, W.G., Rasmussen, C. and Gehrels, G.E. 2021. Magnetostratigraphy of the
1007 Triassic Moenkopi Formation from the continuous cores recovered in Colorado
1008 Plateau Coring Project Phase 1 (CPCP-1), Petrified Forest National Park, Arizona,
1009 USA: correlation of the Early to Middle Triassic strata and biota in Colorado Plateau
1010 and its environs. *Journal of Geophysical Research*, 126,
1011 doi.org/10.1029/2021JB021899.
1012 Heckert, A.B. and Lucas, S.G. 2015. Triassic vertebrate paleontology in New Mexico. *In*:
1013 Lucas, S.G. and Sullivan, R.M. (eds*). Fossil vertebrates in New Mexico*. *New Mexico*
1014 *Museum of Natural History and Science Bulletin*, 68, 77-96.
1015 Hounslow, M.W., 2006. PMagTools version 4.2- a tool for analysis of 2-D and 3-D
1016 directional data. http://dx.doi.org/10.13140/RG.2.2.19872.58880.
1017 Hounslow, M.W. and McIntosh, G. 2003. Magnetostratigraphy of the Sherwood Sandstone
1018 Group (Lower and Middle Triassic), south Devon, UK: detailed correlation of the
1019 marine and non-marine Anisian. *Palaeogeography, Palaeoclimatology,*
1020 *Palaeoecology*, 193, 325-348.
1021 Hounslow, M.W. and Muttoni, G., 2010. The geomagnetic polarity timescale for the Triassic:
1022 linkage to stage boundary definitions. *In*: Lucas, S.G. (ed) *The Triassic timescale*,
1023 Geological Society, London, Special Publications, 334, 61-102.
1024 Hounslow, M.W., Posen, P.E. and Warrington, G., 2004. Magnetostratigraphy and
1025 biostratigraphy of the Upper Triassic and lowermost Jurassic succession, St. Audrie's
1026 Bay, UK. *Palaeogeography, Palaeoclimatology, Palaeoecology*, 213, 331-358.
1027 Hounslow, M.W., Peters, C., Mørk, A., Weitschat, W. and Vigran, J.O. 2008a.
1028 Biomagnetostratigraphy of the Vikinghøgda Formation, Svalbard (Arctic Norway),
1029 and the geomagnetic polarity timescale for the Lower Triassic. *Geological Society of*
1030 *America Bulletin*, 120, 1305-1325.
1031 Hounslow, M.W., Hu, M., Mørk, A., Weitschat, W., Vigran, J.O., Karloukovski, V. and
1032 Orchard, M.J. 2008b. Intercalibration of Boreal and Tethyan time scales: the
1033 magnetobiostratigraphy of the Middle Triassic and the latest Early Triassic from
1034 Spitsbergen, Arctic Norway. *Polar Research*, 27, 469-490.
1035 Hounslow, M.W., Domeier, M. and Biggin, A.J. 2018. Subduction flux modulates the
1036 geomagnetic polarity reversal rate. *Tectonophysics*, 742, 34-49.

1037 Hounslow, M.W., Harris, S.E., Wójcik, K., Nawrocki, J., Woodcock, N.H., Ratcliffe, K.T.
1038 and Montgomery, P. 2021a. Geomagnetic polarity during the early Silurian: The first
1039 magnetostratigraphy of the Llandovery. *Palaeogeography, Palaeoclimatology,*
1040 *Palaeoecology*, 567, doi.org/10.1016/j.palaeo.2021.110245.
1041 Hounslow, M.W. and Carnian-Norian boundary working group, 2021b. Albertiana Working
1042 Group Report: The case for the Global Stratotype Section and Point (GSSP) for the
1043 base of the Norian stage. *Albertiana*, 46, 25-57.
1044 Hounslow, M.W., Harris, S., Karloukovski, V. and Mørk, A. 2022a. Geomagnetic polarity
1045 and carbon isotopic stratigraphic assessment of the late Carnian-earliest Norian in
1046 Svalbard: evidence for a major hiatus and improved Boreal to Tethyan correlation.
1047 *Norwegian Journal of Geology*, 102, https://njg.geologi.no/vol-101-
1048 200/details/30/2339-2339.html
1049 Hounslow, M.W., Xuan, C. and Nilsson. A. 2022b. Chapter 5: Using the geomagnetic field
1050 for correlation and dating. *In:* Coe A.L. (ed). *Deciphering Earth's history: the*
1051 *practice of stratigraphy.* Geological Society of London, 81-99.
1052 Howard, A., Warrington, G., Ambrose, K. and Rees, J. 2008. *A formational framework for*
1053 *the Mercia Mudstone Group (Triassic) of England and Wales*. British Geological
1054 Survey Research Report, RR/08/04.
1055 Indahl, U.G., Næs, T. and Liland, K.H., 2018. A similarity index for comparing coupled
1056 matrices. *Journal of Chemometrics,* 32, doi.org/10.1002/cem.3049.
1057 Irmis, R.B., Martz, J.W., Parker, W.G. and Nesbitt, S.J. 2010. Re-evaluating the correlation
1058 between Late Triassic terrestrial vertebrate biostratigraphy and the GSSP-defined
1059 marine stages. *Albertiana*, 38, pp.40-52.
1060 Irmis, R.B., Mundil, R., Mancuso, A.C., Carrillo-Briceño, J.D., Ottone, E.G. and Marsicano,
1061 C.A. 2022. South American Triassic geochronology: Constraints and uncertainties for
1062 the tempo of Gondwanan non-marine vertebrate evolution. *Journal of South American*
1063 *Earth Sciences,* 116, doi.org/10.1016/j.jsames.2022.103770.
1064 Irving, E. and Runcorn, S.K. 1957. II. Analysis of the paleomagnetism of the Torridonian
1065 sandstone series of North-West Scotland. I. *Philosophical Transactions of the Royal*
1066 *Society of London. Series A, Mathematical and Physical Sciences*, 250, 83-99.
1067 Jeans, C.V. 1978. The origin of the Triassic clay assemblages of Europe with special reference
1068 to the Keuper Marl and Rhaetic of parts of England. *Philosophical Transactions of the*
1069 *Royal Society of London*, Series A, 289, 549-639.

1070 Jefferson, I., Rosenbaum, M., and Smalley, I. 2000. Mercia Mudstone as a Triassic aeolian
1071 desert sediment. *Mercian Geologist,* 15, 157–162.
1072 Jin, X., McRoberts, C.A., Shi, Z., Mietto, P., Rigo, M., Roghi, G., Manfrin, S., Franceschi,
1073 M. and Preto, N. 2019. The aftermath of the CPE and the Carnian–Norian transition in
1074 northwestern Sichuan Basin, South China. *Journal of the Geological Society*, 176,
1075 179-196.
1076 Josse, J., Pagès, J. and Husson, F. 2008. Testing the significance of the RV coefficient.
1077 *Computational Statistics & Data Analysis*, 53, 82-91.
1078 Kent, D.V. and Clemmensen, L.B. 2021. Northward dispersal of dinosaurs from Gondwana
1079 to Greenland at the mid-Norian (215–212 Ma, Late Triassic) dip in atmospheric
1080 pCO_2. *Proceedings of the National Academy of Sciences*, 118,
1081 doi.org/10.1073/pnas.2020778118.
1082 Kent, D.V., Santi Malnis, P., Colombi, C.E., Alcober, O.A. and Martínez, R.N. 2014. Age
1083 constraints on the dispersal of dinosaurs in the Late Triassic from magnetochronology
1084 of the Los Colorados Formation (Argentina). *Proceedings of the National Academy of*
1085 *Sciences*, 111, 7958-7963.
1086 Kent, D.V., Olsen, P.E. and Muttoni, G. 2017. Astrochronostratigraphic polarity time scale
1087 (APTS) for the Late Triassic and Early Jurassic from continental sediments and
1088 correlation with standard marine stages. *Earth-Science Reviews*, 166, 153-180.
1089 Kent, J.T., Briden, J.C. and Mardia, K.V. 1983. Linear and planar structure in ordered
1090 mulivariate data as applied to progressive demagnetisation of palaeomagnetic
1091 remanance. *Geophysical Journal of the Royal Astronomical Society,* 81: 75-87.
1092 Kemp, D.B. and Coe, A.L., 2007. A nonmarine record of eccentricity forcing through the
1093 Upper Triassic of southwest England and its correlation with the Newark Basin
1094 astronomically calibrated geomagnetic polarity time scale from North America.
1095 *Geology*, 35, 991-994.
1096 Kozur, H.W. and Weems, R.E. 2010. The biostratigraphic importance of conchostracans in
1097 the continental Triassic of the northern hemisphere. *In*: Lucas, S.G. (ed) *The Triassic*
1098 *timescale, Geological Society, London, Special Publications*, 334, 315-417.
1099 Krystyn, L., Richoz, S., Gallet, Y., Bouquerel, H., Kürschner, W.M. and Spötl, C. 2007.
1100 Updated bio-and magnetostratigraphy from Steinbergkogel (Austria), candidate GSSP
1101 for the base of the Rhaetian stage. *Albertiana,* 36, 164–173.

1102 Krystyn, L., Mandl, G.W. and Schauer, M. 2009. Growth and termination of the upper
1103 Triassic platform margin of the Dachstein area (northers calcareous alps, Austria).
1104 *Austrian Journal of Earth Sciences*, 102, 23-33.
1105 Kürschner, W.M. and Herngreen, G.W. 2010. Triassic palynology of central and
1106 northwestern Europe: a review of palynofloral diversity patterns and biostratigraphic
1107 subdivisions. *In*: Lucas, S.G. (ed) *The Triassic timescale, Geological Society, London,*
1108 *Special Publications,* 334, 263-283.
1109 Lallier, F., Antoine, C., Charreau, J., Caumon, G. and Ruiu, J. 2013. Management of
1110 ambiguities in magnetostratigraphic correlation. *Earth and Planetary Science Letters*,
1111 371, 26-36.
1112 Lehrmann, D.J., Stepchinski, L., Altiner, D., Orchard, M.J., Montgomery, P., Enos,
1113 Ellwood, B.B., Bowring, S.A., Ramezani, J., Wang, H., Wei, J., Yu, M., Griffiths,
1114 J.D., Minzoni, M., Schaal, E.K., Li, X., Meyer, K.M. and Payne, J.L. 2015. An
1115 integrated biostratigraphy (conodonts and foraminifers) and chronostratigraphy
1116 (paleomagnetic reversals, magnetic susceptibility, elemental chemistry, carbon
1117 isotopes and geochronology) for the Permian–Upper Triassic strata of Guandao
1118 section, Nanpanjiang Basin, south China. *Journal of Asian Earth Sciences,* 108, 117–
1119 135.
1120 Li, M., Huang, C., Hinnov, L., Chen, W., Ogg, J. and Tian, W. 2018. Astrochronology of the
1121 Anisian stage (Middle Triassic) at the Guandao reference section, South China. *Earth*
1122 *and Planetary Science Letters,* 482, 591-606.
1123 Li, Q., Ruhl, M., Wang, Y.D., Xie, X.P., An, P.C. and Xu, Y.Y. 2022. Response of Carnian
1124 Pluvial Episode evidenced by organic carbon isotopic excursions from western Hubei,
1125 South China. *Palaeoworld*, 31, 324-333.
1126 Li, Y., Shi, W., Aydin, A., Beroya-Eitner, M.A. and Gao, G. 2020. Loess genesis and
1127 worldwide distribution. *Earth-Science Reviews,* 201,
1128 doi.org/10.1016/j.earscirev.2019.102947
1129 Lu, J., Zhang, P., Dal Corso, J., Yang, M., Wignall, P.B., Greene, S.E., Shao, L., Lyu, D. and
1130 Hilton, J. 2021. Volcanically driven lacustrine ecosystem changes during the Carnian
1131 Pluvial Episode (Late Triassic). *Proceedings of the National Academy of Sciences,*
1132 118, doi.org/10.1073/pnas.2109895118.

1133 Lucas, S.G., Tanner, L.H., Kozur, H.W., Weems, R.E. and Heckert, A.B. 2012. The Late
1134 Triassic timescale: age and correlation of the Carnian–Norian boundary. *Earth-*
1135 *Science Reviews,* 114, 1-18.
1136 Lucas, S.G. and Schoch, R.R., 2002. Triassic temnospondyl biostratigraphy, biochronology
1137 and correlation of the German Buntsandstein and North American Moenkopi
1138 Formation. Lethaia, 35, 97-106.
1139 Man, O., 2008. On the identification of magnetostratigraphic polarity zones. Studia
1140 *Geophysica et Geodaetica*, 52, 173-186.
1141 Mao, X., Liu, X. and Zhou, X. 2021. Permo-Triassic aeolian red clay of southwestern
1142 England and its palaeoenvironmental implications. *Aeolian Research*, 52,
1143 doi.org/10.1016/j.aeolia.2021.100726
1144 Maron, M., Muttoni, G., Rigo, M., Gianolla, P. and Kent, D.V. 2019. New
1145 magnetobiostratigraphic results from the Ladinian of the Dolomites and implications
1146 for the Triassic geomagnetic polarity timescale. *Palaeogeography,*
1147 *Palaeoclimatology, Palaeoecology*, 517, 52-73.
1148 Martz, J.W. and Parker, W.G., 2017. Revised formulation of the Late Triassic Land
1149 Vertebrate "Faunachrons" of western North America: recommendations for codifying
1150 nascent systems of vertebrate biochronology. In: Ziegler, K.E and Parker, W.G. (eds).
1151 *Terrestrial depositional systems,* 39-125, Elsevier. doi.org/10.1016/B978-0-12-
1152 803243-5.00006-6). Elsevier.
1153 Mazaheri-Johari, M., Gianolla, P., Mather, T.A., Frieling, J., Chu, D. and Dal Corso, J. 2021.
1154 Mercury deposition in Western Tethys during the Carnian Pluvial Episode (Late
1155 Triassic). *Scientific reports*, 11, 1-10.
1156 McKie, T. 2014. Climatic and tectonic controls on Triassic dryland terminal fluvial system
1157 architecture, central North Sea. *In:* Martinius, A.W., Ravnås, R., Howell, J.A., Steel,
1158 R.J. and Wonham, J.P. (eds*) From depositional systems to sedimentary successions*
1159 *on the Norwegian continental margin*. *International Association of Sedimentologists.*
1160 *Special Publication* 46, 19–58.
1161 McKie, T., 2017. Paleogeographic evolution of latest Permian and Triassic salt basins in
1162 Northwest Europe. *In*: Cámara, P., Flinch, J.F., Soto, J.I., Flinch, J.I. and Tari, G.
1163 (eds). *Permo-Triassic Salt Provinces of Europe, North Africa and the Atlantic*
1164 *Margins*, Elsevier, 159-173.

1165 Meyers, S.R. 2019. Cyclostratigraphy and the problem of astrochronologic testing. *Earth-*
1166 *Science Reviews*, 190, 190-223.
1167 Middleton, N.J. 2017. Desert dust hazards: A global review. *Aeolian research*, 24, 53-63.
1168 Mietto, P., Manfrin, S., Preto, N., Rigo, M., Roghi, G., Furin, S., Gianolla, P., Posenato, R.,
1169 Muttoni, G., Nicora, A. and Buratti, N. 2012. The global boundary stratotype section
1170 and point (GSSP) of the Carnian stage (Late Triassic) at Prati di Stuores/Stuores
1171 Wiesen section (Southern Alps, NE Italy). *Episodes*, 35, 414-430.
1172 Miller, C.S., Peterse, F., Da Silva, A.C., Baranyi, V., Reichart, G.J. and Kürschner, W.M.,
1173 2017. Astronomical age constraints and extinction mechanisms of the Late Triassic
1174 Carnian crisis. *Scientific Reports*, 7, 1-7.
1175 Milner, A.R., Gardiner, B.G., Fraser, N.C. and Taylor, M.A. 1990. Vertebrates from the
1176 Middle Triassic Otter Sandstone Formation of Devon. *Palaeontology*, 33, 873-892.
1177 Milroy, P., Wright, V.P. and Simms, M.J. 2019. Dryland continental mudstones: Deciphering
1178 environmental changes in problematic mudstones from the Upper Triassic (Carnian to
1179 Norian) Mercia Mudstone Group, south-west Britain. *Sedimentology*, 66, 2557-2589.
1180 Morton, A., Hounslow, M.W. and Frei, D. 2013. Heavy-mineral, mineral-chemical and
1181 zircon-age constraints on the provenance of Triassic sandstones from the Devon coast,
1182 southern Britain. *Geologos,* 19, 67–85. doi: 10.2478/logos-2013-0005.
1183 Mueller, S., Hounslow, M.W. and Kürschner, W.M. 2016. Integrated stratigraphy and
1184 palaeoclimate history of the Carnian Pluvial Event in the Boreal realm; new data from
1185 the Upper Triassic Kapp Toscana Group in central Spitsbergen (Norway). *Journal of*
1186 *the Geological Society*, 173, 186-202.
1187 Muttoni, G., Kent, D.V., Olsen, P.E., Stefano, P.D., Lowrie, W., Bernasconi, S.M. and
1188 Hernández, F.M. 2004. Tethyan magnetostratigraphy from Pizzo Mondello (Sicily)
1189 and correlation to the Late Triassic Newark astrochronological polarity time scale.
1190 *Geological Society of America Bulletin*, 116, 1043-1058.
1191 Nawrocki, J. and Szulc, J. 2000. The Middle Triassic magnetostratigraphy from the Peri-
1192 Tethys basin in Poland. *Earth and Planetary Science Letters*, 182, 77-92.
1193 Nawrocki, J., Jewuła, K., Stachowska, A. and Szulc, J. 2015. Magnetic polarity of Upper
1194 Triassic sediments of the Germanic Basin in Poland. *Annales Societatis Geologorum*
1195 *Poloniae*, 85, 663-674, doi: 10.14241/asgp.2015.026

1196 Newell, A.J. 2018a. Evolving stratigraphy of a Middle Triassic fluvial-dominated sheet
1197 sandstone: The Otter Sandstone Formation of the Wessex Basin (UK). *Geological*
1198 *Journal,* 53, 1954-1972.
1199 Newell, A.J. 2018b. Rifts, rivers and climate recovery: A new model for the Triassic of
1200 England. *Proceedings of the Geologists' Association*, 129, 352-371.
1201 Nitsch, E., Beutler, G., Hauschke, N., Etzold, A. and Laass, M. 2005. Feinstratigraphische
1202 Korrelation der Grabfeld-Formation (Keuper, Trias) zwischen Hochrhein und Ostsee.
1203 *Hallesches Jahrbuch für Geowissenschaften, Reihe B: Geologie, Paläontologie,*
1204 *Mineralogie,* 19, 137-152.
1205 Ogg, J.G., Chen, Z.Q., Orchard, M.J. and Jiang, H.S. 2020. The Triassic Period. *In:*
1206 Gradstein, F.M., Ogg, J.G., Schmitz, M.D. and Ogg, G.M. (eds), *Geologic Time Scale*
1207 *2020,* Elsevier, 903-953. DOI: https://doi.org/10.1016/B978-0-12-824360-2.00025-5.
1208 Olson, P., Hinnov, L.A. and Driscoll, P.E., 2014. Nonrandom geomagnetic reversal times and
1209 geodynamo evolution. *Earth and Planetary Science Letters*, 388, 9-17.
1210 Paul, J., Wemmer, K. and Ahrendt, H. 2008. Provenance of siliciclastic sediments (Permian
1211 to Jurassic) in the Central European Basin. *Zeitschrift der Deutschen Gesellschaft fur*
1212 *Geowissenschaften*, **159**, 641-650
1213 Porter, R.J. and Gallois, R.W. 2008. Identifying fluvio–lacustrine intervals in thick playa-lake
1214 successions: An integrated sedimentology and ichnology of arenaceous members in
1215 the mid–late Triassic Mercia Mudstone Group of south-west England, UK.
1216 *Palaeogeography, Palaeoclimatology, Palaeoecology*, 270, 381-398.
1217 Rayfield, E.J., Barrett, P.M. and Milner, A.R., 2009. Utility and validity of Middle and Late
1218 Triassic 'land vertebrate faunachrons'. *Journal of Vertebrate Paleontology*, 29, 80-87.
1219 Reinhardt, L. and Ricken, W. 2000. The stratigraphic and geochemical record of Playa
1220 Cycles: monitoring a Pangaean monsoon-like system (Triassic, Middle Keuper, S.
1221 Germany). *Palaeogeography, Palaeoclimatology, Palaeoecology*, 161, 205-227.
1222 Rigo, M., Bertinelli, A., Concheri, G., Gattolin, G., Godfrey, L., Katz, M.E., Maron, M.,
1223 Mietto, P., Muttoni, G., Sprovieri, M. and Stellin, F., 2016. The Pignola-Abriola
1224 section (southern Apennines, Italy): a new GSSP candidate for the base of the
1225 Rhaetian Stage. *Lethaia*, 49, 287-306.
1226 Rigo, M., Mazza, M., Karádi, V. and Nicora, A., 2018. New Upper Triassic conodont
1227 biozonation of the Tethyan realm. *In*: Tanner, L. (eds) *The Late Triassic World*.
1228 Springer, Cham, 189-235. doi.org/10.1007/978-3-319-68009-5_6

1229 Ruffell, A., Simms, M.J. and Wignall, P.B. 2016. The Carnian humid episode of the Late
1230 Triassic: a review. *Geological Magazine*, 153, 271-284.
1231 Seyfullah, L.J., Kustatscher, E. and Taylor, W.A. 2013. The first discovery of in situ
1232 *Verrucosisporites applanatus* spores from the Middle Triassic flora from Bromsgrove
1233 (Worcestershire, UK). *Review of Palaeobotany and Palynology*, 197, 15-25.
1234 Song, H., Wignall, P.B. and Dunhill, A.M. 2018. Decoupled taxonomic and ecological
1235 recoveries from the Permo-Triassic extinction. *Science advances*, 4, doi.org/
1236 10.1126/sciadv.aat509.
1237 Spencer, P.S. and Storrs, G.W. 2002. A re-evaluation of small tetrapods from the Middle
1238 Triassic Otter Sandstone Formation of Devon, England. *Palaeontology*, 45, 447-467.
1239 Stockar, R., Baumgartner, P.O. and Condon, D. 2012. Integrated Ladinian bio-
1240 chronostratigraphy and geochrononology of Monte San Giorgio (Southern Alps,
1241 Switzerland). *Swiss Journal of Geosciences,* 105, 85-108.
1242 Sun, Y.D., Orchard, M.J., Kocsis, Á.T. and Joachimski, M.M. 2020. Carnian–Norian (Late
1243 Triassic) climate change: Evidence from conodont oxygen isotope thermometry with
1244 implications for reef development and Wrangellian tectonics. *Earth and Planetary*
1245 *Science Letters,* 534, doi.org/10.1016/j.epsl.2020.116082.
1246 Swanson-Hysell, N.L., Fairchild, L.M. and Slotznick, S.P. 2019. Primary and secondary red
1247 bed magnetization constrained by fluvial intraclasts. *Journal of Geophysical*
1248 *Research*, *Solid Earth*, 124, 4276-4289.
1249 Szurlies, M. 2007. Latest Permian to Middle Triassic cyclo-magnetostratigraphy from the
1250 Central European Basin, Germany: Implications for the geomagnetic polarity
1251 timescale. *Earth and Planetary Science Letters,* 261, 602-619.
1252 Tanner, L.H. and Lucas, S.G. 2015. The Triassic-Jurassic strata of the Newark Basin, USA: a
1253 complete and accurate astronomically-tuned timescale. *Stratigraphy*, 12, 47-65.
1254 Talbot, M., Holm, K. and Williams, M. 1994. Sedimentation in low-gradient desert margin
1255 systems: A comparison of the Late Triassic of northwest Somerset. In: Rosen, M.R.
1256 (ed). *Paleoclimate and basin evolution of playa systems*, *Geological Society of*
1257 *America special paper*, 289, 97-118.
1258 Vollmer, T., Werner, R., Weber, M., Tougiannidis, N., Röhling, H.G. and Hambach, U. 2008.
1259 Orbital control on Upper Triassic Playa cycles of the Steinmergel-Keuper (Norian): A
1260 new concept for ancient playa cycles. *Palaeogeography, Palaeoclimatology,*
1261 *Palaeoecology,* 267, 1-16.

1262 Wang, M., Li, M., Kemp, D.B., Boulila, S. and Ogg, J.G. 2022. Sedimentary noise modeling
1263 of lake-level change in the Late Triassic Newark Basin of North America. *Global and*
1264 *Planetary Change*, 208, page numbers. doi.org/10.1016/j.gloplacha.2021.103706.
1265 Warrington, G. H., 1971. Palynology of the New Red Sandstone of the South Devon coast.
1266 *Proceedings of the Ussher Society* 2, 307-314.
1267 Warrington, G. H. 1997. The Lyme Regis Borehole, Dorset-palynology of the Mercia
1268 Mudstone, Penarth and Lias groups (Upper Triassic-Lower Jurassic). *Proceedings of*
1269 *the Ussher Society*, 9, 153-157.
1270 Warrington, G. 2005. The chronology of the Permian and Triassic of Devon and south-east
1271 Cornwall (U.K.): a review of methods and results. *Geoscience in south-west England*,
1272 11, 117-122.
1273 Withjack, M.O., Schlische, R.W., Malinconico, M.L. and Olsen, P.E. 2013. Rift-basin
1274 development: lessons from the Triassic–Jurassic Newark Basin of eastern North
1275 America. *In*: W. U. Mohriak, A. Danforth, P. J. Post, D. E. Brown, G. C. Tari, M.
1276 Nemčok, S. T. Sinha (eds.). *Conjugate Divergent Margins. Geological Society,*
1277 *London, Special Publications,* 369, 301-321.
1278 Wójcik, K., Kołbuk, D., Sobień, K., Rosowiecka, O., Roszkowska-Remin, J., Nawrocki, J.
1279 and Szymkowiak, A. 2017. Keuper magnetostratigraphy in the southern Mesozoic
1280 margin of the Holy Cross Mts. (southeastern edge of the German Basin). *Geological*
1281 *Quarterly*, 61, 946-961.
1282 Zeigler, K.E. and Geissman, J.W. 2011. Magnetostratigraphy of the Upper Triassic Chinle
1283 Group of New Mexico: Implications for regional and global correlations among
1284 Upper Triassic sequences. *Geosphere*, 7, 802-829.
1285 Zhang, Y., Ogg, J.G., Franz, M., Bachmann, G.H., Szurlies, M., Röhling, H.G., Li, M., Rolf,
1286 C. and Obst, K. 2020. Carnian (Late Triassic) magnetostratigraphy from the Germanic
1287 Basin allowing global correlation of the Mid-Carnian Episode. *Earth and Planetary*
1288 *Science Letters*, 541, doi.org/10.1016/j.epsl.2020.116275.
1289 Zhang, Z.T., Sun, Y.D., Lai, X.L., Joachimski, M.M. and Wignall, P.B., 2017. Early Carnian
1290 conodont fauna at Yongyue, Zhenfeng area and its implication for Ladinian-Carnian
1291 subdivision in Guizhou, South China. *Palaeogeography, Palaeoclimatology,*
1292 *Palaeoecology*, 486, 142-157.

Figure Captions

Fig. 1. Geological sketch sections of the Mercia Mudstone Group outcrop in the cliffs between Sidmouth in the west and Bindon Cliffs (east of Seaton). All sections projected onto a west-east line. Drift deposits and minor landslides omitted for clarity. Inset shows location in UK.

Fig. 2. Summary of the magnetostratigraphic data for the Sidmouth to Salcombe Mouth section. A) simplified sedimentary log (see SI Fig. S1.1 for detailed log) and magnetic susceptibility (MS) and initial natural remanent magnetisation (NRM) intensity (each point represents a demagnetised specimen). B) Demagnetisation behaviour classification of specimen data. C) Specimen polarity classification. D) Virtual geomagnetic pole latitude (VGP_R) with respect to the formation mean pole, with S-class data with filled symbol and T-class data with unfilled symbol; E) interpreted polarity and section lithostratigraphy. MZ=labels of magnetozone couplets (BS8r is a continuation of that used by Hounslow and McIntosh (2003) for the Budleigh Salterton to Sidmouth Section); SS=Sidmouth to Seaton sections.

Fig. 3. Summary magnetostratigraphic data for the Salcombe Mouth to Hook Ebb section. See Fig. 2 for column details. See SI Fig. S1.2 for detailed log.

Fig. 4. Summary magnetostratigraphic data for the Strangman's Cove section. See Fig. 2 for column details. The position of the organic matter carbon isotope excursions of Miller et al. (2017) and Baranyi et al. (2019) are shown as (C). See SI Fig. S1.3 for detailed log.

Fig. 5. Summary magnetostratigraphic data for the Littlecombe Shoot sections. Upper panels are the western section, and lower panels the eastern section. See Fig. 2 for column details. See SI Fig. S1.4 for detailed log. DMF=Dunscombe Mudstone Fm.

Fig. 6. Summary magnetostratigraphic data for the Red Rock to Branscombe Mouth section. See Fig. 2 for column details. See SI Figs S1.4 and S1.5 for detailed logs.

Fig. 7. Summary magnetostratigraphic data for the Seaton Cliff section. See Fig. 2 for column details. See SI Fig.S1.6 for detailed log.

Fig. 8. Summary magnetostratigraphic data for the Haven Cliff section. See Fig. 2 for column details. See SI Fig. S1.7 for detailed log.

Fig. 9. Specimen S-class ChRM directions for the sections. A) Sidmouth Mudstone Fm and Pennington Point Member from the Sid outfall to Hook Ebb sections. B) The Strangman's Cove section, largely in the Dunscombe Mudstone Formation; C) The

Littlecombe Shoot sections in the Littlecombe Shoot Mudstone Member. D) The Red Rock Gypsum and Seaton Mudstone Members in the Branscombe Mouth and Seaton Cliffs sections; E) Haven Cliff section. See SI Table S3.1 for mean directions and other directional tests.

Fig. 10. Magnetic polarity correlations for the interval from the middle part of the Otter Sandstone Fm and lower part of the Sidmouth Mudstone Fm. GPTS-A from Maron et al. (2019), Ogg et al. (2020) and GPTS-B from Hounslow and Muttoni (2010). Otter Sandstone data from Hounslow and McIntosh (2003), with lithostratigraphy of Newell (2018a) and Gallois (2001). PPM= Pennington Point Member. See text for description of option-1 and option-2 correlations. Details of the statistical comparisons are in the SI.

Fig. 11. Correlation of the upper part of the Sidmouth Mudstone Fm to the Erfurt to Grabfeld formations of the Central European Basin (Morsleben polarity from Zhang et al. 2020). Likely correlation to the GPTS composites of Hounslow and Muttoni (2010) and Maron et al. (2019) are indicated. The differences between the two GTPS are related to the differences in correlation between the marine Stoures and Mayerling sections. GPTS-B uses that proposed by Broglio Loriga et al. (1999), GPTS-A use the first occurrence of the conodont *Paragondolella polygnathiformis* (Mietto et al. 2012; a single specimen at Stuores). The base of Julian-2 (J2) in GPTS-A is based on conodonts in Zhang et al. (2017), and in GPTS-B conodonts of Gallet et al. (1998).

Fig. 12. Comparison of the magnetostratigraphy of the Carnian-age interval of the MMG with the GPTS-A of Ogg et al. (2020) and GPTS-B of Hounslow et al. (2022a). The correlation of the Morsleben core data to the GPTS-A is that of Zhang et al. (2020). Position of negative carbon isotope excursions (C) shown are based on Fig. 5 for the MMG excursions (labelled DIE# on MMG column), Hounslow et al. (2022a) for the Tuvalian-Lacian excursions (CIE, T1 to T6 & L1), and Dal Corso et al. (2018) and Mueller et al. (2016) for the Julian excursions (J1- J4 on GPTS-A).

Fig. 13. Comparison of the Dunscombe Mudstone Fm (DMF) to the cycles and magnetostratigraphy of the Morsleben cores. Bed labels on DMF from Gallois and Porter (2006). Cycles in Morsleben 52a from Barnasch (2010), and lithostratigraphy from Franz et al. (2014). Red arrows are possible sequence stratigraphic correlations. Seq.= sequence stratigraphy outlined in SI Table S1.2.

Fig. 14. Summary data for composite magnetostratigraphy through the Norian and early Rhaetian, modified from Hounslow and Muttoni (2010) (see SI section 5 for source details). See SI Fig. S5.3, S5.4 and SI section 5.1 for details of the upper Chinle Formation composite and detrital zircon ages. Newark Supergroup magnetostratigraphy from Kent et al. (2017), with astronomically anchored ages from their table 3. Red arrowed bar is the estimated stratigraphic uncertainty range in placing the radiometric date of Furin et al. (2006) onto the magnetostratigraphy. *E. quadrata* (*E. abneptis* A) and *E. slovakensis* (*E. n. sp*. D) conodont biozones are from Krystyn et al. (2009), others from Rigo et al. (2018). Fleming Fjord and La Sal section data from Kent and Clemmenson (2021) and Kent et al. (2014) respectively. Radioisotopic dates below La Sal section described in Irmis et al. (2022).

Fig. 15. Correlation of the magnetostratigraphy of the Norian-Rhaetian part of the MMG to the GPTS-B from Fig. 14. The likely missing interval in the Newark Supergroup in the middle of the E14 magnetozone is explained in the text. NRB1 and NRB2 are the positions proposed for the base of the Rhaetian of Krystyn et al. (2007) and Rigo et al. (2016) respectively. Magnetostratigraphic composite for upper Chinle Fm from SI Fig. S5.4. St Audrie's Bay data from Hounslow et al. (2004).

Fig. 16. The accumulation rates for the Otter Sandstone Fm and the Mercia Mudstone Group, using three age models. Symbols represent 'instantaneous' accumulation rates using the magnetochron durations, and the lines are geometric means of three adjacent instantaneous accumulation rates. Abbreviations: -M= Member, -MM= Mudstone Member, PP= Pennington Point, SH=Salcombe Hill; SM=Salcombe Mouth; HE=Hook Ebb; LW=Little Weston, LS=Littlecombe Shoot; RRG=Red Rock Gypsum; S= Seaton, HC=Haven Cliff; BAF=Blue Anchor.

Formation	**Member [thickness, metres]**	**Type locality**
Blue Anchor Fm (BAF)	[c. 30 incomplete] on Devon coast	Blue Anchor, Somerset
Branscombe Mudstone Fm (BMF)	Haven Cliff Mudstone Mb [20]	Haven Cliff
	Seaton Mudstone Mb [c.115 incomplete]	Branscombe Mouth to Seaton
	Red Rock Gypsum Mb [9.5]	Red Rock
	Littlecombe Shoot Mudstone Mb [78.6 incomplete]	Littlecombe Shoot
Dunscombe Mudstone Fm (DMF)	[35.7 incomplete[1]]	Strangman's Cove
Sidmouth Mudstone Fm (SMF)	Little Weston Mudstone Mb [34.6]	Hook Ebb
	Hook Ebb Mudstone Mb [63.4]	Salcombe Mouth to Hook Ebb
	Salcombe Mouth Siltstone Mb [11.0]	Salcombe Mouth
	Salcombe Hill Mudstone Mb [60.5]	Salcombe Hill to Salcombe Mouth
	Sid Mudstone Mb [15.5]	Sid outfall to Salcombe Hill
Otter Sandstone Fm (Sherwood Sandstone Group)	Pennington Point Mb [22]	Pennington Point (Sid outfall)

Table 1. Lithostratigraphic subdivision of the Mercia Mudstone Group exposed on the Devon coast (after Gallois, 2001, 2019).

Fm=Formation; Mb= Member. [1]Later sections have shown up to 41 m for the DMF.

.

Section [site code]	Section thickness (m)	Thickness sampled (m)	N/Ns	Grid Reference
Haven Cliff [HC]	67 (unknown gap at base, c 6 m gap at top)	60	164/81	SY2565 8972-SY 2730 8936
Seaton Cliff [SE]	29 (unknown gaps at base and top)	19.5	30/17	SY2382 8979
Red Rock- Branscombe Mouth [MB]	64; (c. 15m gap at base, unknown gap at top)	64	40/30	SY1984 8807-SY2029 8815
Littlecombe Shoot east [SH]	31	25	20/10	SY1800 8799-SY1984 8807
Littlecombe Shoot west [ML]	39	37	28/20	SY1691 8793-SY1800 8799
Strangman's Cove [MW]	61	57	93/44	SY 1691 8793
Salcombe Mouth-Hook Ebb [MD]	70	55	27/19	SY1462 8765-SY1566 8776
Sid Outfall-Salcombe Mouth [MS]	102	98	45/41	SY1290 8733-SY1462 8765
Total	463 plus gaps	~361	447/262	

Table 2. Summary of magnetostratigraphic sampling from the Mercia Mudstone Group, Sidmouth to Haven Cliff. Thicknesses are those shown on the SI FigsS1.1 to S1.7. Localities shown on Fig. 1, and details in SI Table S3.1. N=Number of specimens ;Ns= Number of sampled horizons.

Reference GPTS	**Comparison**	**Fig.**	**SMI, PSI, P_{RV}**	**Nc, d_{median}**	**Absent/ extra magnetozones**
GPTS-A (Option-1); GD4r-MA5n	BS3r-SS3n	11	0.53,0.64,<0.001	24, 0.73	SC4r.1n, SC4r.2n, SC2r.1n, SC2r.2n / BS3r.1n BS4n, BS4r,
GPTS-A (Option-2); GD4r-MA5n	BS3r-SS3n	11	0.37,0.59, 0.002	22, 0.74	GD6n,GD6r, SC2r.1n, SC4r.1n, SC4r.2n/ BS7n.2r, BS7n.1n, BS7r
GPTS-B ; MT4r-UT1n	BS3r-SS3n	11	0.42,0.67, <0.001	24, 0.48	MT7n.1r, MT8r.1n, MT11r.1n, MT11r.2n/ BS4n SS2r.1n,SS2r.2r.
GPTS-A ; GD4n- MA5n	GPTS-B; MT4n-UT1n	11	0.78,0.91, <0.001	31, 0.37	MT5n/ MA3r, MA4n
Morsleben;MK3r.1r-MK5r.1r	SS3r-SS6r	13	0.64,0.54, 0.47	9, 0.92	MK5r.1n/ SS6r.1n, SS7n
GPTS-A; WY1n.2r-E9r	SS3r-SS8r	13	0.52, 0.58, 0.046	15, 0.91	E2r,E3r,E4r,E5n.1r/none
GPTS-B ; UT4n-UT14r	SS3r.1n- SS8r	13	0.51, 0.72, <0.001	14, 0.77	UT6n-UT9n, UT11r.1n, UT11n.1r, UT12r.1n, UT13n.1r/ none
GPTS-B ; UT4n- UT14r	GPTS-A; WY1r.1r-E9r	13	0.4, 0.52, 0.030	20, 0.71	UT8n, UT11n.1r, UT11r.1n, UT12r.1n, UT13n.1r / E15n.1r
GPTS-B ; UT13r.2r- UT24n	SS7r—HC3r.1n	16	0.42, 0.65, <0.001	28, 0.84	None/ SS9r.1n, SS9r.3n
Chinle; CC1n-CC9r.2r	SS8n- HC3r	16	0.36, 0.49, 0.014	26, 1.08	CC3n, CC3r.1n, CC6r.1n / SS9r.1n, SS9r.3n, SS12n.1r, HC2n.1r, HC3r.1n
Newark ATS; E9r-E20n	Chinle; CC1r.1r-CC9r.2n	16	0.36, 0.65, <0.001	26, 0.87	E13n.1r/ CC5n.1r, CC5n.2n, CC5r.1n, CC6n.1r,
GPTS-B ; UT14r- UT24n	Chinle; CC1r.1r-CC9r.2n	16	0.48, 0.80, <0.001	30, 0.66	None/ CC5r.1n

Table 3. Statistics for the comparison of magnetic polarity correlation models in this work. The reference and comparison are the polarity patterns correlated, as shown in the figure number, using the magnetozone/chron ranges indicated. SMI, PSI= similarity of matrices index and Procrustes similarity index determined as in Indahl et al. (2018), with ranges 0-1.0 (no to perfect similarity). P_{RV}= the RV-based statistic testing the probability of association between the two sets (<0.05=strong association) as in Josse et al. (2007). d_{median}= median Euclidean distance of the number of magnetozones/chrons in the comparison (Nc), larger d_{median} correspond to larger average divergence. Absent/extra= magnetozones absent from the reference GPTS set used/ additional magnetozones in the comparison set not shown in the reference set. See SI for data details.

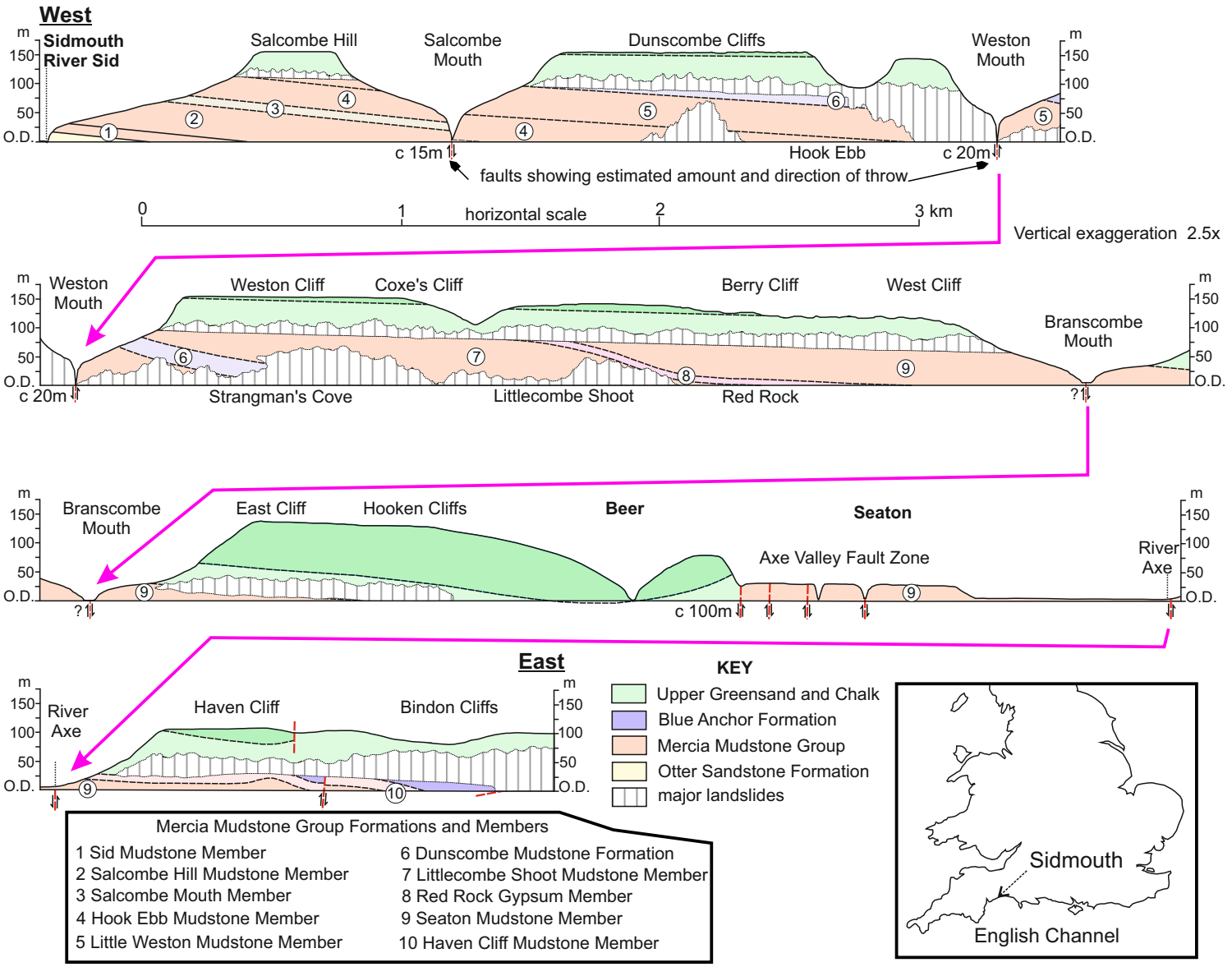
West
Sidmouth
River Sid
Salcombe Hill
Salcombe Mouth
Dunscombe Cliffs
Weston Mouth
m
150
100
50
O.D.
c 15m
Hook Ebb
c 20m
faults showing estimated amount and direction of throw
0
1
horizontal scale
2
3 km
Vertical exaggeration 2.5x
Weston Mouth
Weston Cliff
Coxe's Cliff
Berry Cliff
West Cliff
Branscombe Mouth
c 20m
Strangman's Cove
Littlecombe Shoot
Red Rock
?
East Cliff
Hooken Cliffs
Beer
Seaton
Axe Valley Fault Zone
River Axe
c 100m
East
Haven Cliff
Bindon Cliffs
KEY
Upper Greensand and Chalk
Blue Anchor Formation
Mercia Mudstone Group
Otter Sandstone Formation
major landslides
Sidmouth
English Channel
Mercia Mudstone Group Formations and Members
1 Sid Mudstone Member
2 Salcombe Hill Mudstone Member
3 Salcombe Mouth Member
4 Hook Ebb Mudstone Member
5 Little Weston Mudstone Member
6 Dunscombe Mudstone Formation
7 Littlecombe Shoot Mudstone Member
8 Red Rock Gypsum Member
9 Seaton Mudstone Member
10 Haven Cliff Mudstone Member

Fig. 1

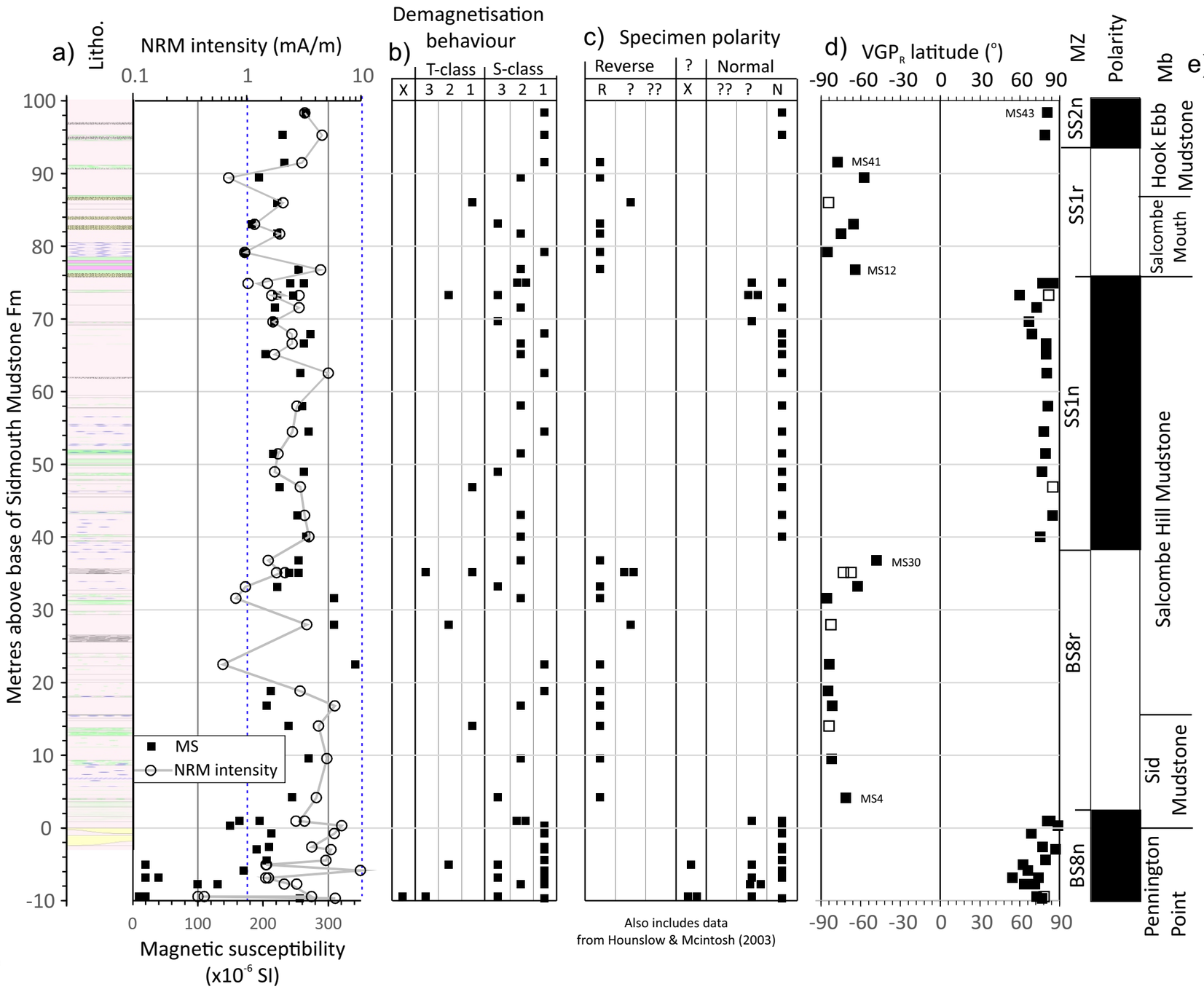
a)
Litho.
NRM intensity (mA/m)
0.1
1
10
b)
Demagnetisation behaviour
T-class
S-class
X
3 2 1
3 2 1
c)
Specimen polarity
Reverse
?
Normal
R ? ??
X
?? ? N
d)
VGP$_R$ latitude (°)
-90 -60 -30 0 30 60 90
MZ
Polarity
Mb
e)
Metres above base of Sidmouth Mudstone Fm
100
90
80
70
60
50
40
30
20
10
0
-10
MS43
MS41
MS12
MS30
MS4
SS2n
SS1r
SS1n
BS8r
BS8n
Hook Ebb Mudstone
Salcombe Mouth
Salcombe Hill Mudstone
Sid Mudstone
Pennington Point
MS
NRM intensity
0
100
200
300
Magnetic susceptibility
(x10^{-6} SI)
Also includes data
from Hounslow & Mcintosh (2003)
-90 -60 -30 0 30 60 90

Fig. 2

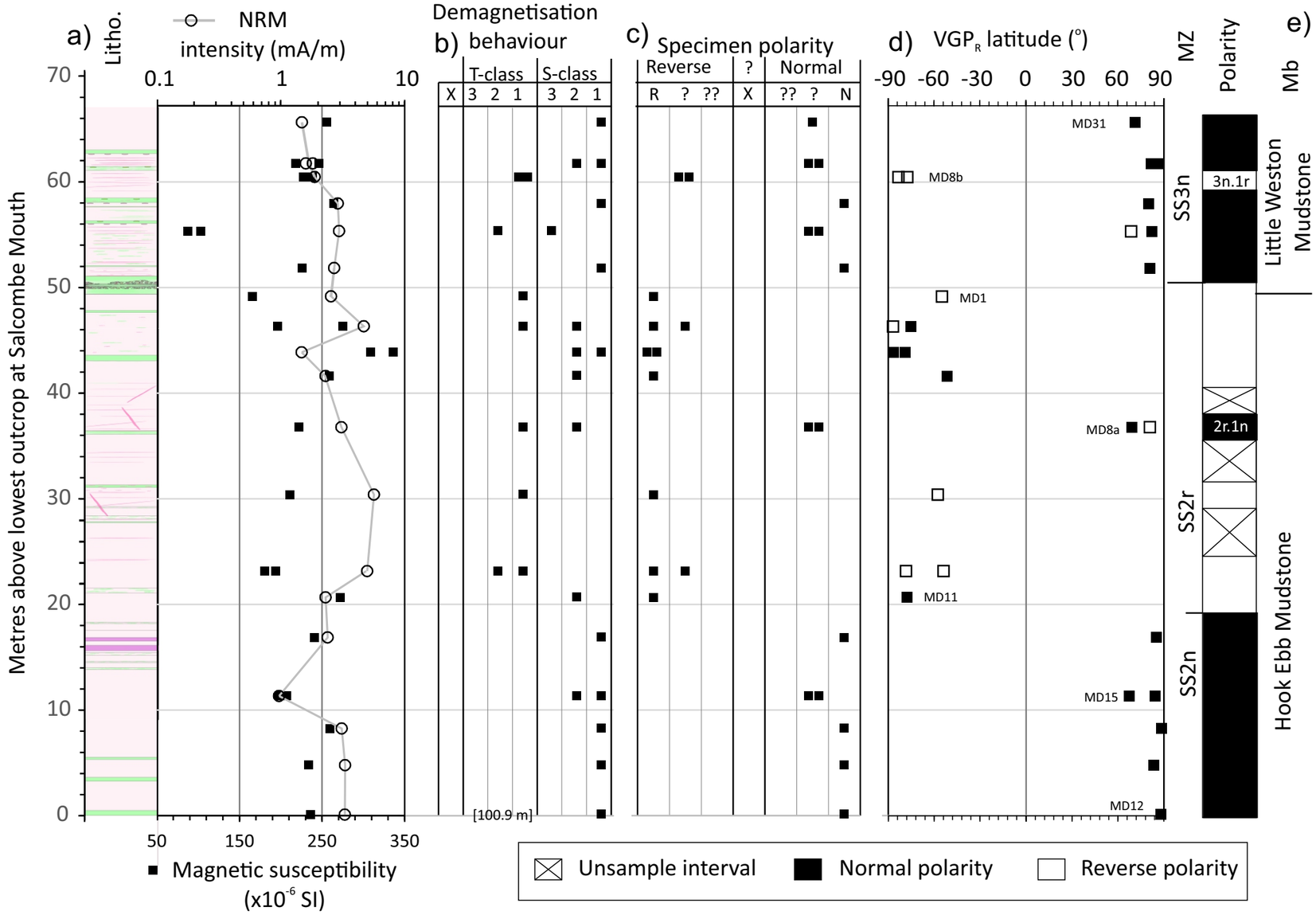
a)
Litho.
NRM intensity (mA/m)
0.1
1
10
b)
Demagnetisation behaviour
T-class
S-class
X 3 2 1 3 2 1
c)
Specimen polarity
Reverse
?
Normal
R ? ?? X ?? ? N
d)
VGP$_R$ latitude (°)
-90 -60 -30 0 30 60 90
MZ
Polarity
e)
Mb
Metres above lowest outcrop at Salcombe Mouth
70
60
50
40
30
20
10
0
MD31
MD8b
MD1
MD8a
MD11
MD15
MD12
[100.9 m]
SS3n
3n.1r
Little Weston Mudstone
2r.1n
SS2r
SS2n
Hook Ebb Mudstone
50 150 250 350
Magnetic susceptibility (x10^{-6} SI)
Unsample interval
Normal polarity
Reverse polarity

Fig. 3

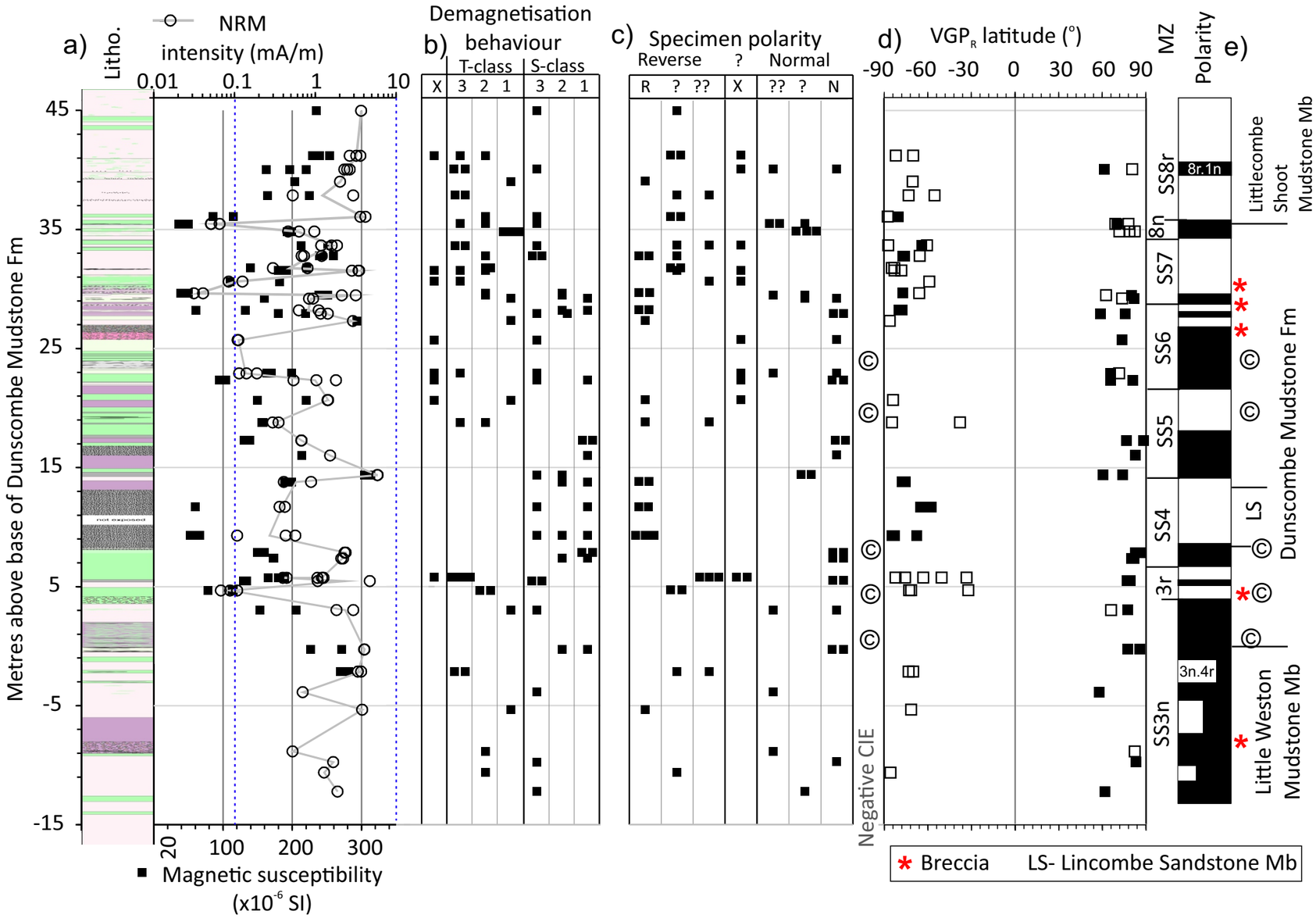
a)
Litho.
NRM intensity (mA/m)
0.01
0.1
1
10
b)
Demagnetisation behaviour
T-class
S-class
X
3 2 1
3 2 1
c)
Specimen polarity
Reverse
?
Normal
R ? ??
X
?? ? N
d)
VGP$_R$ latitude (°)
-90 -60 -30 0 30 60 90
MZ
Polarity
e)
Littlecombe Shoot Mudstone Mb
Dunscombe Mudstone Fm
LS
Little Weston Mudstone Mb
SS8r
8r.1n
8n
SS7
SS6
SS5
SS4
3r
3n.4r
SS3n
Negative CIE
Metres above base of Dunscombe Mudstone Fm
45
35
25
15
5
-5
-15
not exposed
20
100
200
300
Magnetic susceptibility (x10^{-6} SI)
* Breccia
LS- Lincombe Sandstone Mb

Fig. 4

Fig. 5

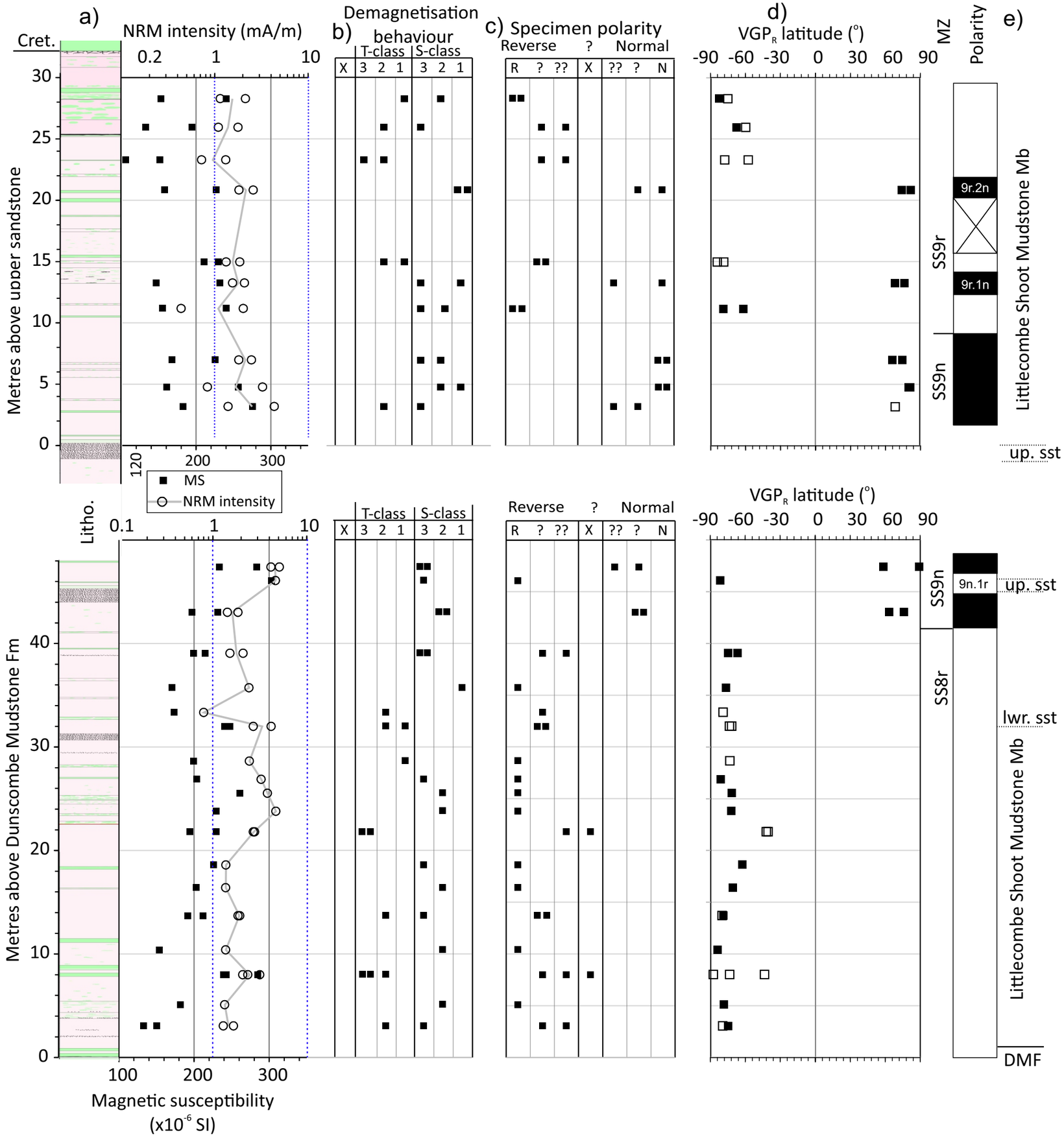
a)
NRM intensity (mA/m)
Cret.
Metres above upper sandstone
MS
NRM intensity
b)
Demagnetisation behaviour
T-class
S-class
c) Specimen polarity
Reverse
Normal
d)
VGP$_R$ latitude (°)
MZ
e)
Polarity
9r.2n
9r.1n
SS9r
SS9n
Littlecombe Shoot Mudstone Mb
up. sst
Litho.
Metres above Dunscombe Mudstone Fm
9n.1r
SS8r
lwr. sst
DMF
Magnetic susceptibility
(x10^{-6} SI)

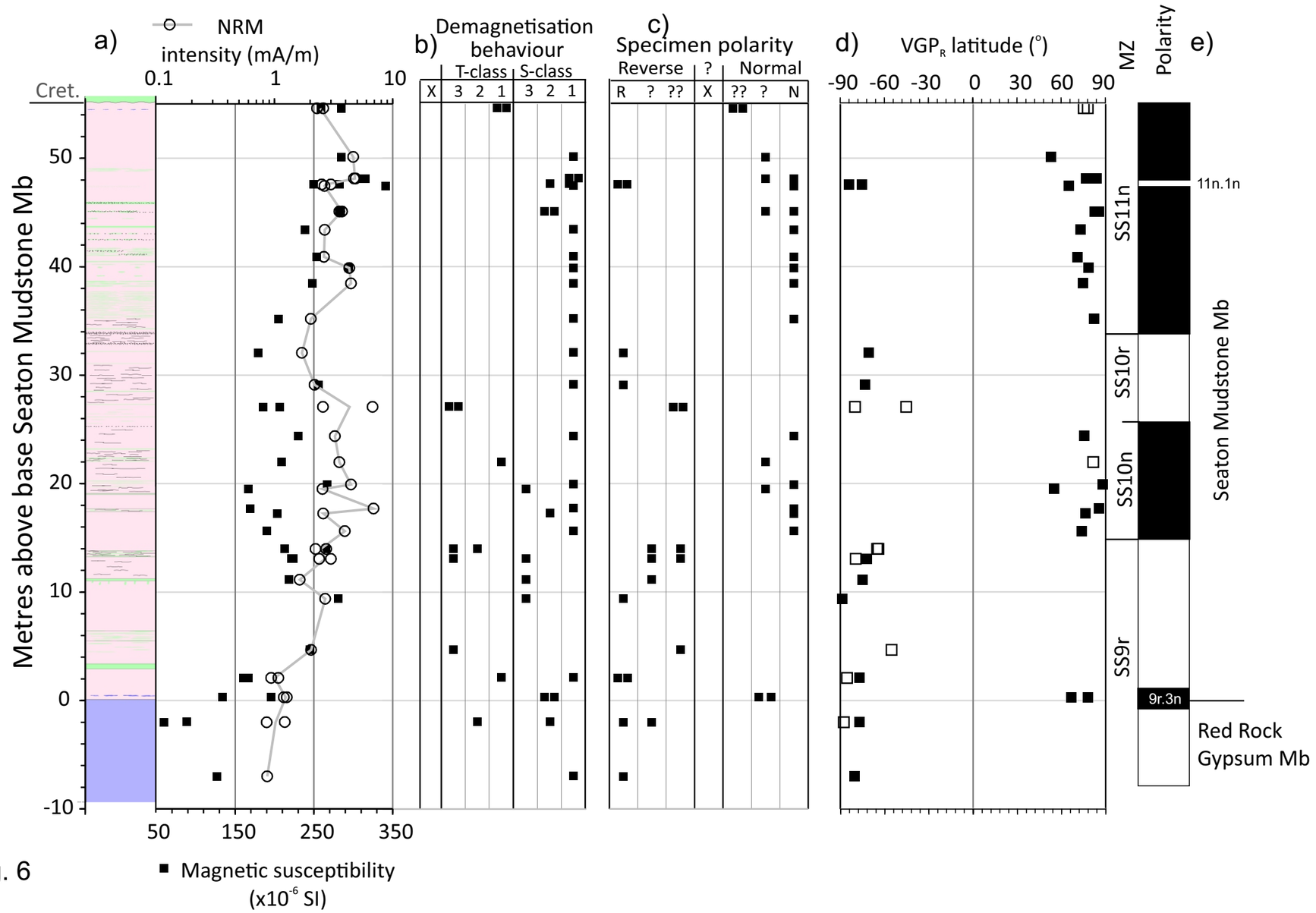
a)
NRM intensity (mA/m)
0.1
1
10
b)
Demagnetisation behaviour
T-class
S-class
X
3 2 1
3 2 1
c)
Specimen polarity
Reverse
?
Normal
R ? ??
X
?? ? N
d)
VGP$_R$ latitude (°)
-90 -60 -30 0 30 60 90
MZ
Polarity
e)
Cret.
Metres above base Seaton Mudstone Mb
50
40
30
20
10
0
-10
50 150 250 350
Magnetic susceptibility (x10^{-6} SI)
SS11n
SS10r
SS10n
SS9r
11n.1n
9r.3n
Seaton Mudstone Mb
Red Rock Gypsum Mb

Fig. 6

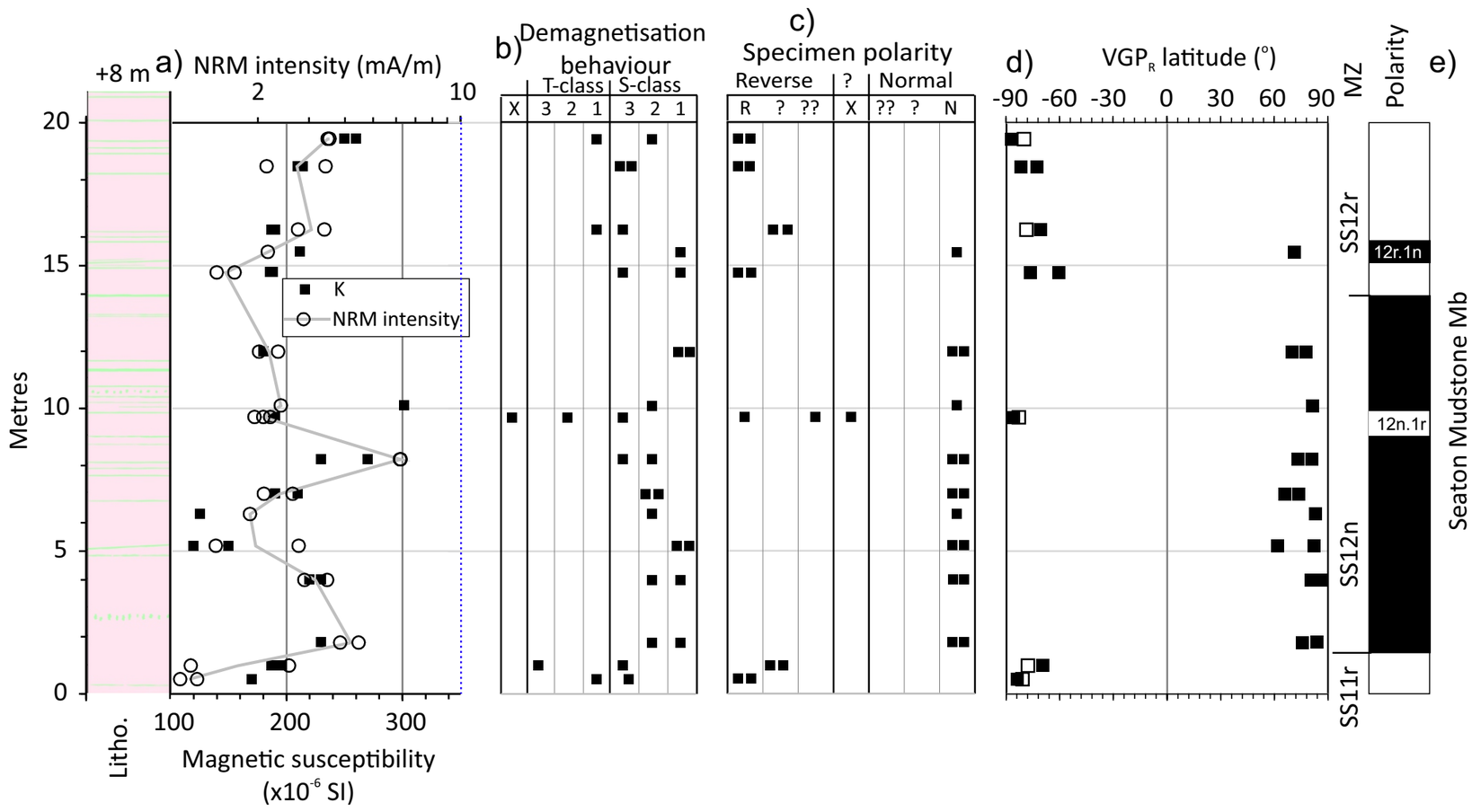
+8 m
a) NRM intensity (mA/m)
2
10
b) Demagnetisation behaviour
T-class
S-class
X 3 2 1 3 2 1
c) Specimen polarity
Reverse
?
Normal
R ? ?? X ?? ? N
d) VGP$_R$ latitude (°)
-90 -60 -30 0 30 60 90
MZ
Polarity
e)
20
15
10
5
0
Metres
K
NRM intensity
SS12r
12r.1n
12n.1r
SS12n
SS11r
Seaton Mudstone Mb
Litho.
100
200
300
Magnetic susceptibility
(x10^{-6} SI)

Fig. 7

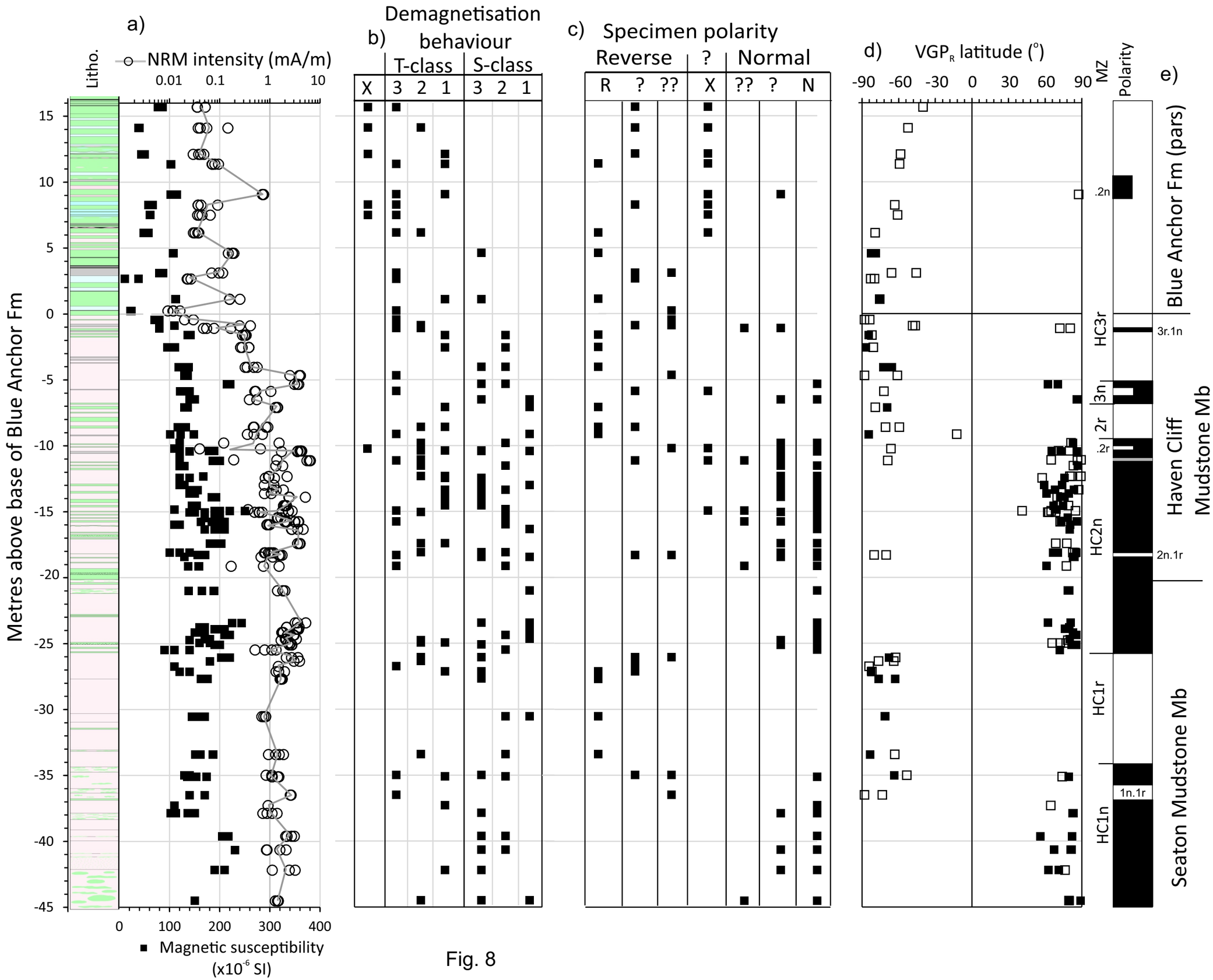
a)
Litho.
NRM intensity (mA/m)
0.01
0.1
1
10
Metres above base of Blue Anchor Fm
15
10
5
0
-5
-10
-15
-20
-25
-30
-35
-40
-45
0
100
200
300
400
Magnetic susceptibility
(x10-6 SI)
b)
Demagnetisation behaviour
T-class
S-class
X
3
2
1
3
2
1
c)
Specimen polarity
Reverse
?
Normal
R
?
??
X
??
?
N
d)
VGP$_R$ latitude (°)
-90
-60
-30
0
30
60
90
MZ
Polarity
e)
.2n
HC3r
3r.1n
3n
2r
.2r
HC2n
2n.1r
HC1r
1n.1r
HC1n
Blue Anchor Fm (pars)
Haven Cliff Mudstone Mb
Seaton Mudstone Mb

Fig. 8

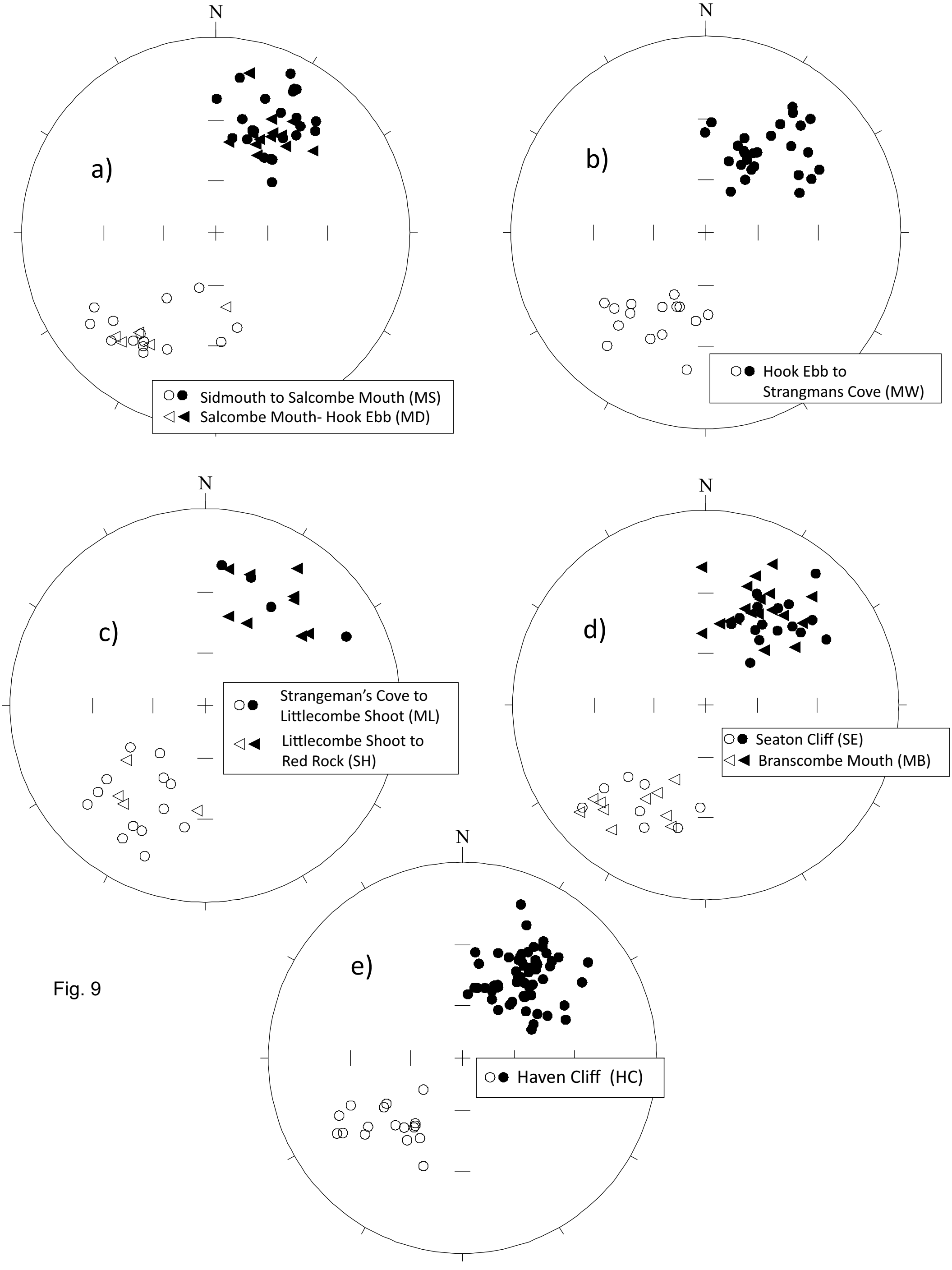
N
a)
Sidmouth to Salcombe Mouth (MS)
Salcombe Mouth- Hook Ebb (MD)
N
b)
Hook Ebb to
Strangmans Cove (MW)
N
c)
Strangeman's Cove to
Littlecombe Shoot (ML)
Littlecombe Shoot to
Red Rock (SH)
N
d)
Seaton Cliff (SE)
Branscombe Mouth (MB)
N
e)
Haven Cliff (HC)

Fig. 9

Fig. 10

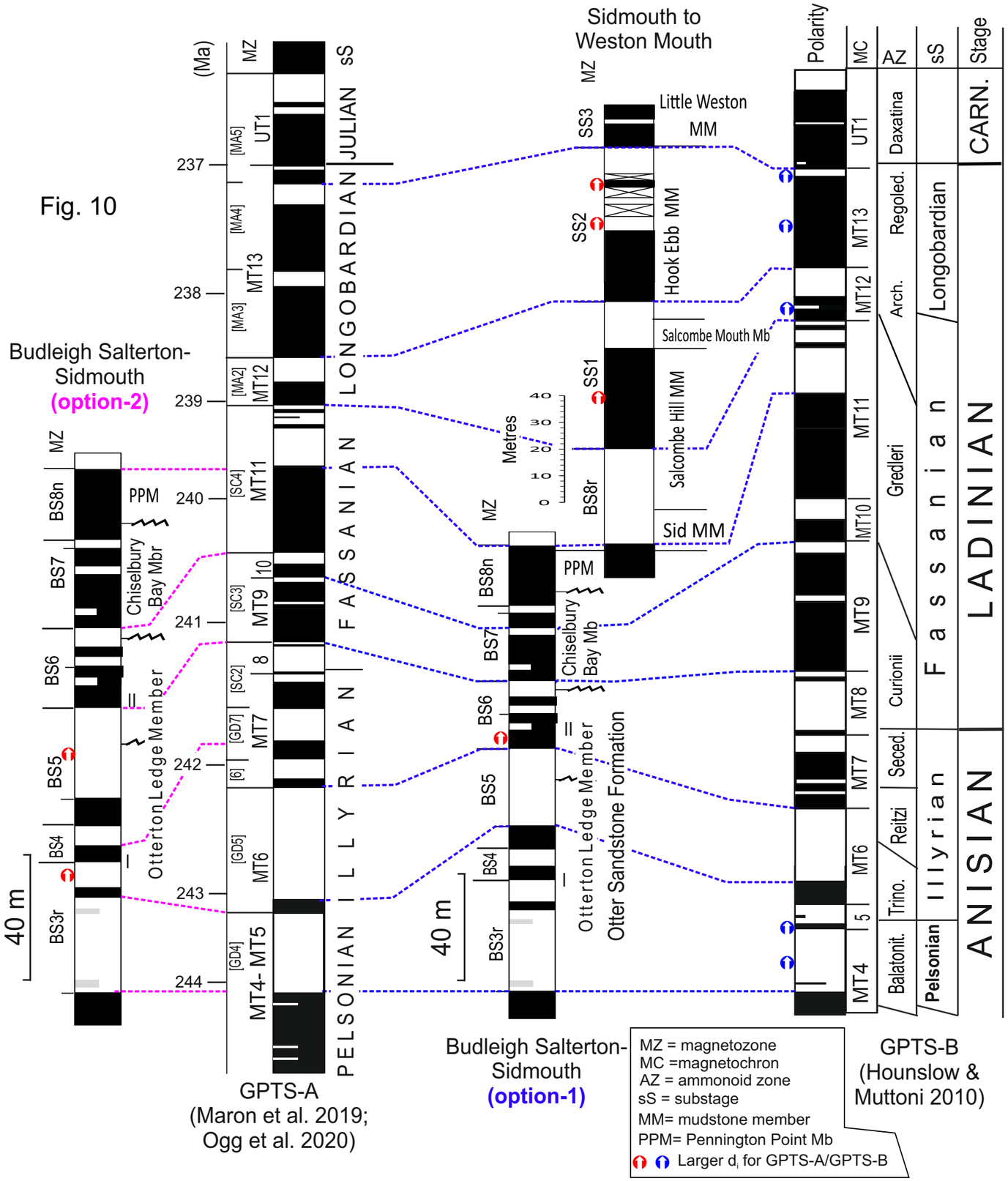
Budleigh Salterton-
Sidmouth
(option-2)
(Ma)
MZ
sS
237
238
239
240
241
242
243
244
[MA5]
[MA4]
[MA3]
[MA2]
[SC4]
[SC3]
[SC2]
[GD7]
[6]
[GD5]
[GD4]
UT1
MT13
MT12
MT11
MT9
MT7
MT6
MT4- MT5
10
8
JULIAN
LONGOBARDIAN
FASSANIAN
ILLYRIAN
PELSONIAN
BS8n
BS7
BS6
BS5
BS4
BS3r
PPM
Chiselbury Bay Mbr
Otterton Ledge Member
40 m
GPTS-A
(Maron et al. 2019;
Ogg et al. 2020)
Sidmouth to
Weston Mouth
Little Weston MM
Hook Ebb MM
Salcombe Mouth Mb
Salcombe Hill MM
Sid MM
SS3
SS2
SS1
Metres
Chiselbury Bay Mb
Otter Sandstone Formation
Budleigh Salterton-
Sidmouth
(option-1)
Polarity
MC
AZ
sS
Stage
UT1
MT13
MT12
MT11
MT10
MT9
MT8
MT7
MT6
5
MT4
Daxatina
Regoled.
Arch.
Gredleri
Curionii
Seced.
Reitzi
Trino.
Balatonit.
Pelsonian
Longobardian
Fassanian
Illyrian
CARN.
LADINIAN
ANISIAN
MZ = magnetozone
MC =magnetochron
AZ = ammonoid zone
sS = substage
MM= mudstone member
PPM= Pennington Point Mb
Larger d$_i$ for GPTS-A/GPTS-B
GPTS-B
(Hounslow &
Muttoni 2010)

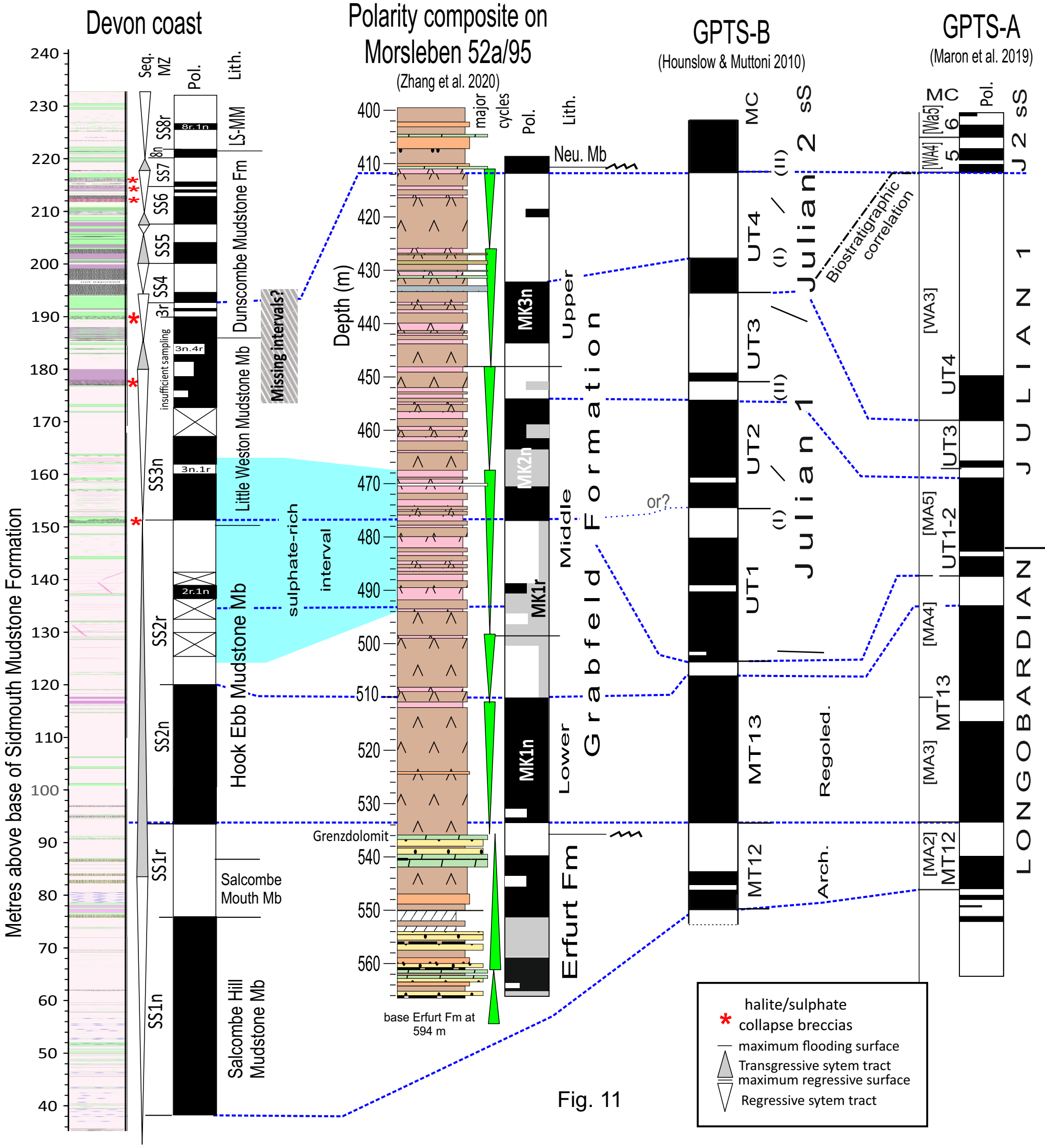
Devon coast
Polarity composite on Morsleben 52a/95
(Zhang et al. 2020)
GPTS-B
(Hounslow & Muttoni 2010)
GPTS-A
(Maron et al. 2019)
Metres above base of Sidmouth Mudstone Formation
Depth (m)
Seq. MZ
Pol.
Lith.
major cycles
SS8r
SS7
SS6
SS5
SS4
SS3n
SS2r
SS2n
SS1r
SS1n
8r.1n
3r
3n.4r
3n.1r
2r.1n
LS-MM
Dunscombe Mudstone Fm
Little Weston Mudstone Mb
Hook Ebb Mudstone Mb
Salcombe Mouth Mb
Salcombe Hill Mudstone Mb
Missing intervals?
insufficient sampling
sulphate-rich interval
Neu. Mb
MK3n
MK2n
MK1r
MK1n
Upper Grabfeld Formation
Middle Grabfeld Formation
Lower Grabfeld Formation
Erfurt Fm
Grenzdolomit
base Erfurt Fm at 594 m
or?
Biostratigraphic correlation
MC
UT4
UT3
UT2
UT1
MT13
MT12
Regoled.
Arch.
Julian 2 sS
Julian 1
JULIAN 1
LONGOBARDIAN
[WA5]
[WA4]
[WA3]
[MA5]
[MA4]
[MA3]
[MA2]
UT1-2
halite/sulphate collapse breccias
maximum flooding surface
Transgressive sytem tract
maximum regressive surface
Regressive sytem tract

Fig. 11

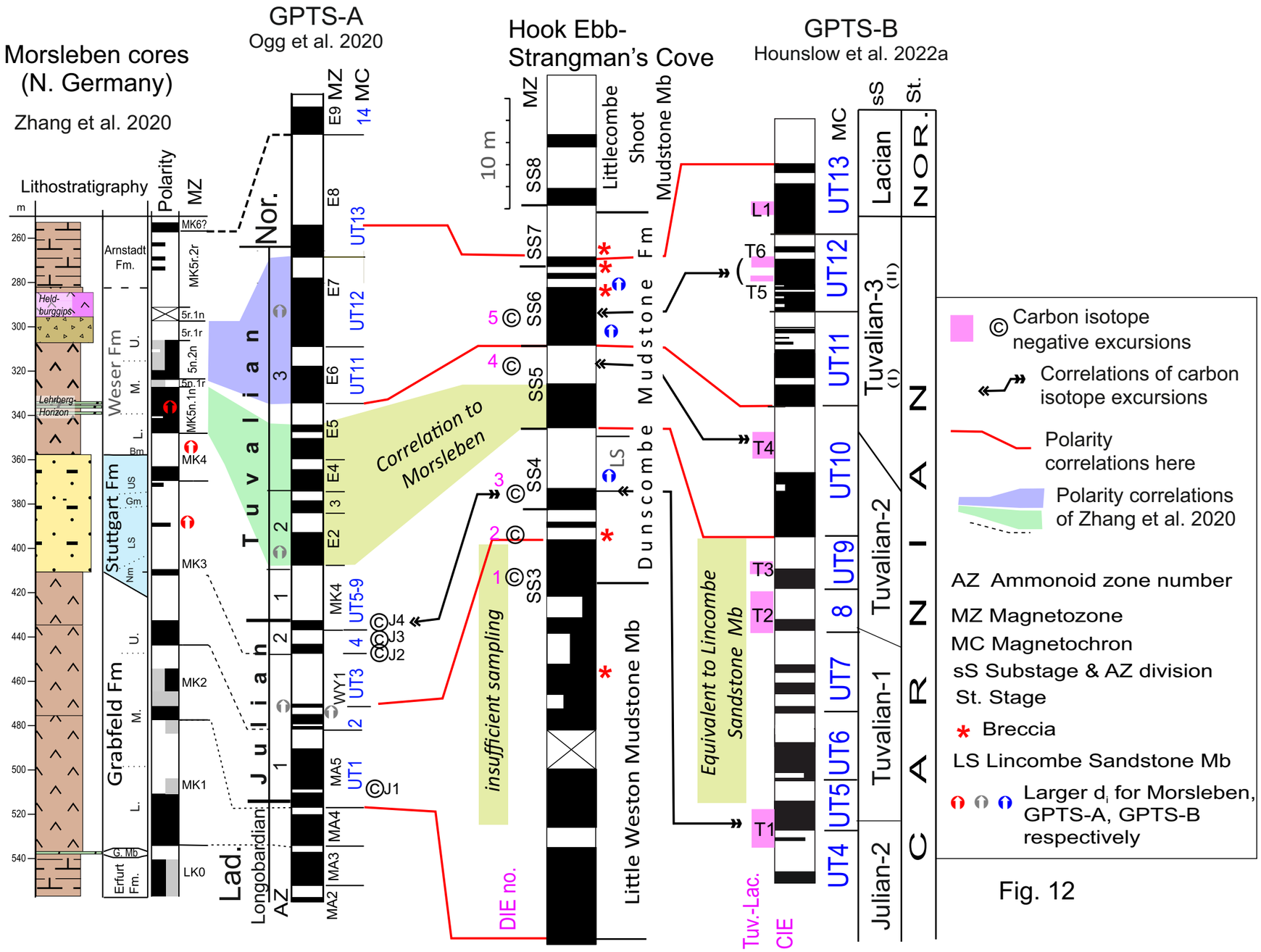
Morsleben cores
(N. Germany)
Zhang et al. 2020
Lithostratigraphy
Polarity
MZ
GPTS-A
Ogg et al. 2020
Hook Ebb-
Strangman's Cove
GPTS-B
Hounslow et al. 2022a
Correlation to Morsleben
insufficient sampling
Equivalent to Lincombe Sandstone Mb
Littlecombe Shoot Mudstone Mb
Dunscombe Mudstone Fm
Little Weston Mudstone Mb
Arnstadt Fm.
Weser Fm
Stuttgart Fm
Grabfeld Fm
Erfurt Fm.
Heldburggips
Lehrberg-Horizon
G. Mb
Nor.
Tuvalian
Julian
Ladinian
Longobardian
AZ
DIE no.
Tuv.-Lac.
CIE
Lacian
Tuvalian-3
Tuvalian-2
Tuvalian-1
Julian-2
sS
St.
NORIAN
CARNIAN
Carbon isotope negative excursions
Correlations of carbon isotope excursions
Polarity correlations here
Polarity correlations of Zhang et al. 2020
AZ Ammonoid zone number
MZ Magnetozone
MC Magnetochron
sS Substage & AZ division
St. Stage
Breccia
LS Lincombe Sandstone Mb
Larger di for Morsleben, GPTS-A, GPTS-B respectively

Fig. 12

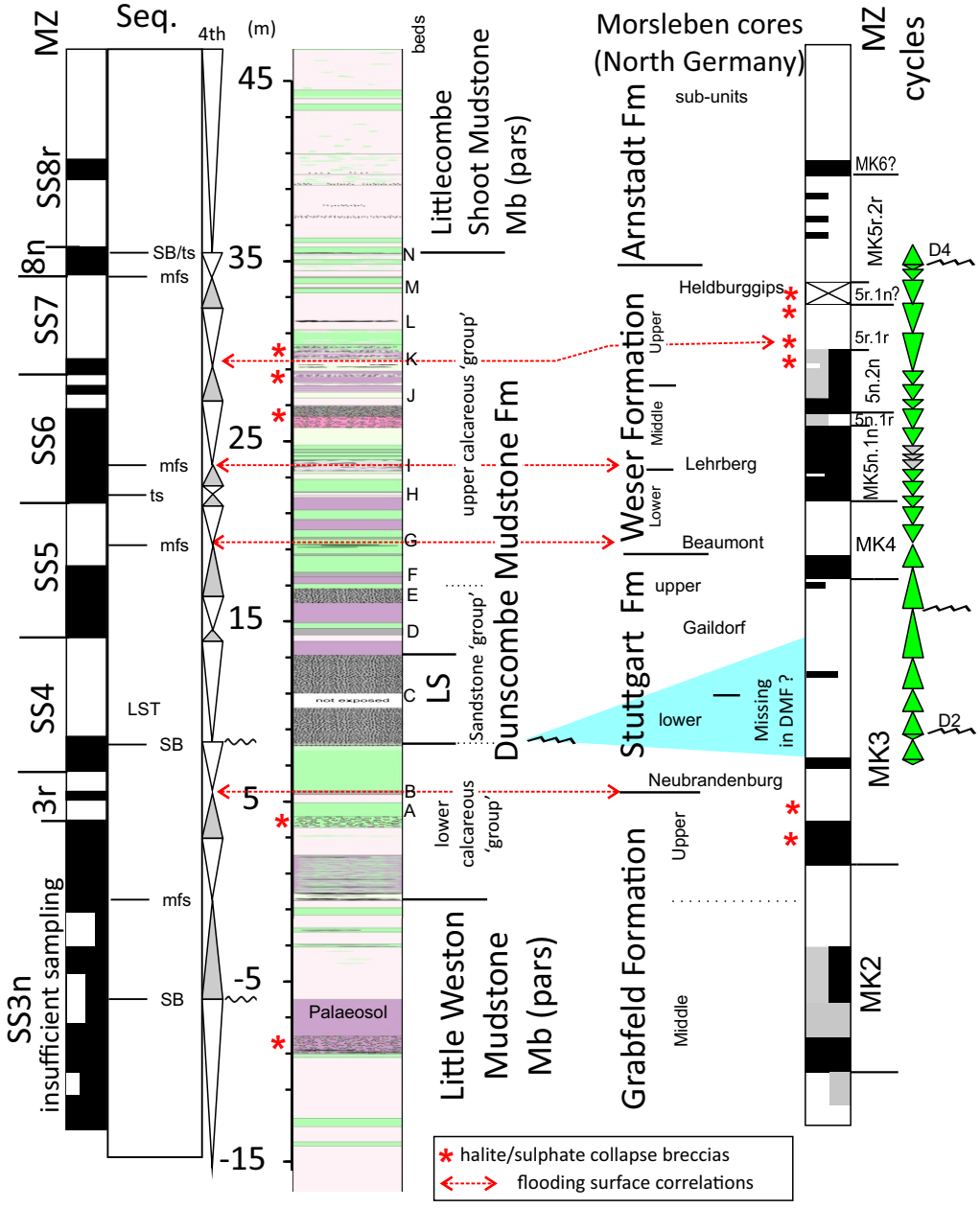
MZ
Seq.
4th
(m)
beds
Littlecombe Shoot Mudstone Mb (pars)
Morsleben cores (North Germany)
MZ cycles
SS8r
8n
SS7
SS6
SS5
SS4
3r
SS3n
insufficient sampling
SB/ts
mfs
mfs
ts
mfs
LST
SB
mfs
SB
45
35
25
15
5
-5
-15
N
M
L
K
J
I
H
G
F
E
D
C
B
A
not exposed
LS
Sandstone 'group'
upper calcareous 'group'
lower calcareous 'group'
Palaeosol
Dunscombe Mudstone Fm
Little Weston Mudstone Mb (pars)
Arnstadt Fm
sub-units
Heldburggips
Weser Formation
Upper
Middle
Lower
Lehrberg
Beaumont
Stuttgart Fm
upper
Gaildorf
lower
Missing in DMF ?
Neubrandenburg
Grabfeld Formation
Upper
Middle
MK6?
MK5r.2r
5r.1n?
5r.1r
5n.2n
5n.1r
MK5n.1n
MK4
MK3
MK2
D4
D2
halite/sulphate collapse breccias
flooding surface correlations

Fig. 13

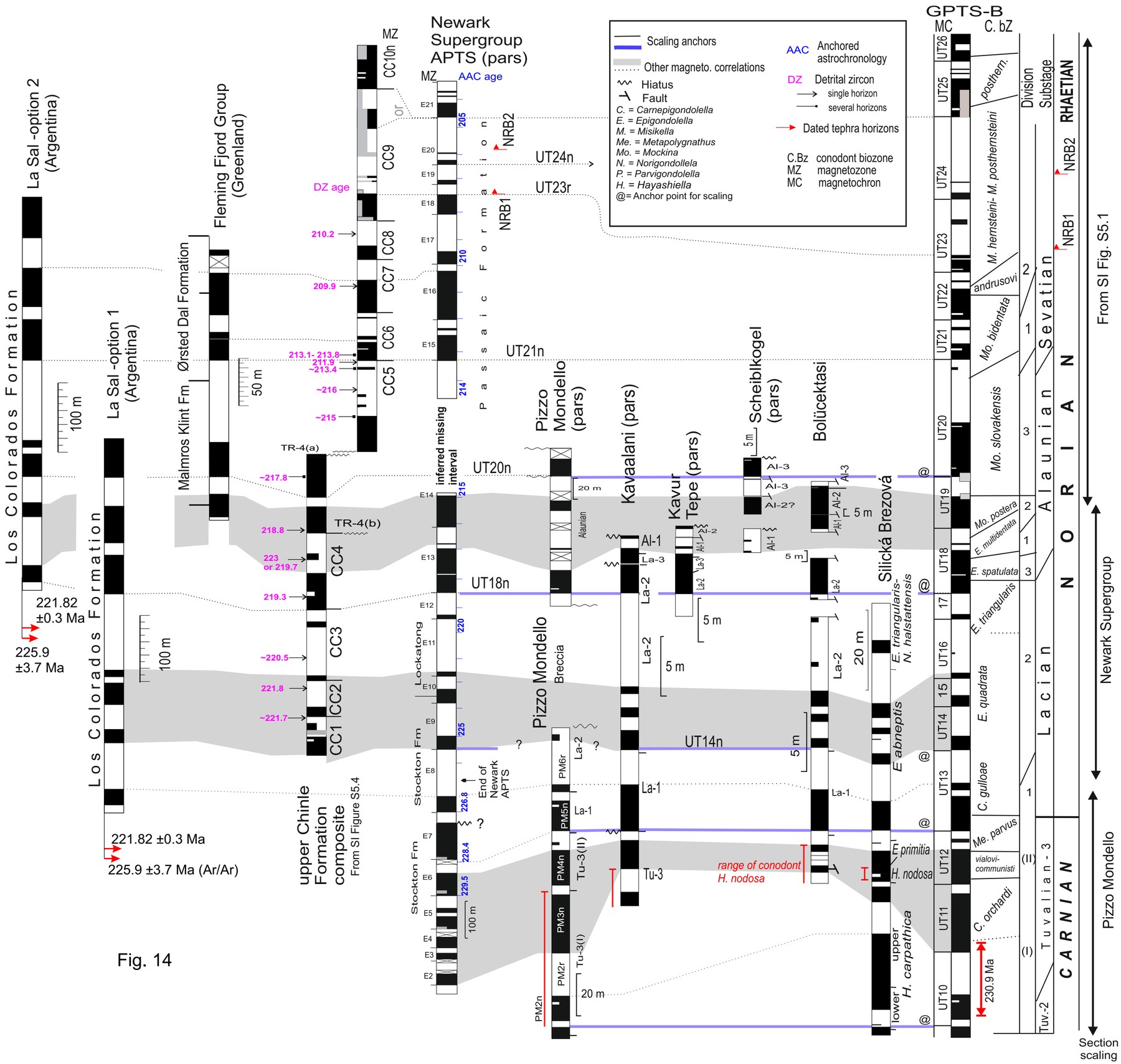
La Sal -option 2 (Argentina)
Los Colorados Formation
100 m
La Sal -option 1 (Argentina)
221.82 ±0.3 Ma
225.9 ±3.7 Ma
Fleming Fjord Group (Greenland)
Ørsted Dal Formation
Mälmros Klint Fm
50 m
MZ
CC10n
CC9
CC8
CC7
CC6
CC5
CC4
CC3
CC2
CC1
DZ age
210.2
209.9
213.1- 213.8
211.9
~213.4
~216
~215
TR-4(a)
~217.8
TR-4(b)
218.8
223 or 219.7
219.3
~220.5
221.8
~221.7
100 m
Los Colorados Formation
221.82 ±0.3 Ma
225.9 ±3.7 Ma (Ar/Ar)
upper Chinle Formation composite
From SI Figure S5.4
Newark Supergroup APTS (pars)
MZ
AAC age
E21
E20
E19
E18
E17
E16
E15
E14
E13
E12
E11
E10
E9
E8
E7
E6
E5
E4
E3
E2
205
210
214
215
220
225
226.8
228.4
229.5
Passaic Formation
NRB2
NRB1
inferred missing interval
Lockatong
Stockton Fm
Stockton Fm
End of Newark APTS
100 m
UT24n
UT23r
UT21n
UT20n
UT18n
UT14n
Pizzo Mondello (pars)
20 m
Alaunian
Pizzo Mondello Breccia
PM6r
PM5n
PM4n
PM3n
PM2r
PM2n
Tu-3(II)
Tu-3(I)
Tu-3
20 m
Kavaalani (pars)
Kavur Tepe (pars)
Al-1
La-3
La-2
La-1
5 m
Scheiblkogel (pars)
Al-3
Al-2?
5 m
Bolücektasi
Al-3
Al-2
Al-1
5 m
La-2
20 m
La-1
5 m
range of conodont
H. nodosa
Silická Brezová
E. triangularis-
N. halstattensis
E abneptis
E primitia
H. nodosa
upper
lower
H. carpathica
Scaling anchors
Other magneto. correlations
Hiatus
Fault
C. = Carnepigondolella
E. = Epigondolella
M. = Misikella
Me. = Metapolygnathus
Mo. = Mockina
N. = Norigondolella
P. = Parvigondolella
H. = Hayashiella
@= Anchor point for scaling
AAC Anchored astrochronology
DZ Detrital zircon
single horizon
several horizons
Dated tephra horizons
C.Bz conodont biozone
MZ magnetozone
MC magnetochron
GPTS-B
MC
C. bZ
UT26
UT25
UT24
UT23
UT22
UT21
UT20
UT19
UT18
UT17
UT16
UT15
UT14
UT13
UT12
UT11
UT10
posthern.
M. hernsteini- M. posthernsteini
andrusovi
Mo. bidentata
Mo. slovakensis
Mo. postera
E. multidentata
E. spatulata
E. triangularis
E. quadrata
C. gulloae
Me. parvus
vialovi-communisti
C. orchardi
230.9 Ma
Division
Substage
RHAETIAN
NRB2
NRB1
Sevatian
ORIAN
Alaunian
Laciian
CARNIAN
Tuvalian-3
Tuv.-2
From SI Fig. S5.1
Newark Supergroup
Pizzo Mondello
Section scaling

Fig. 14

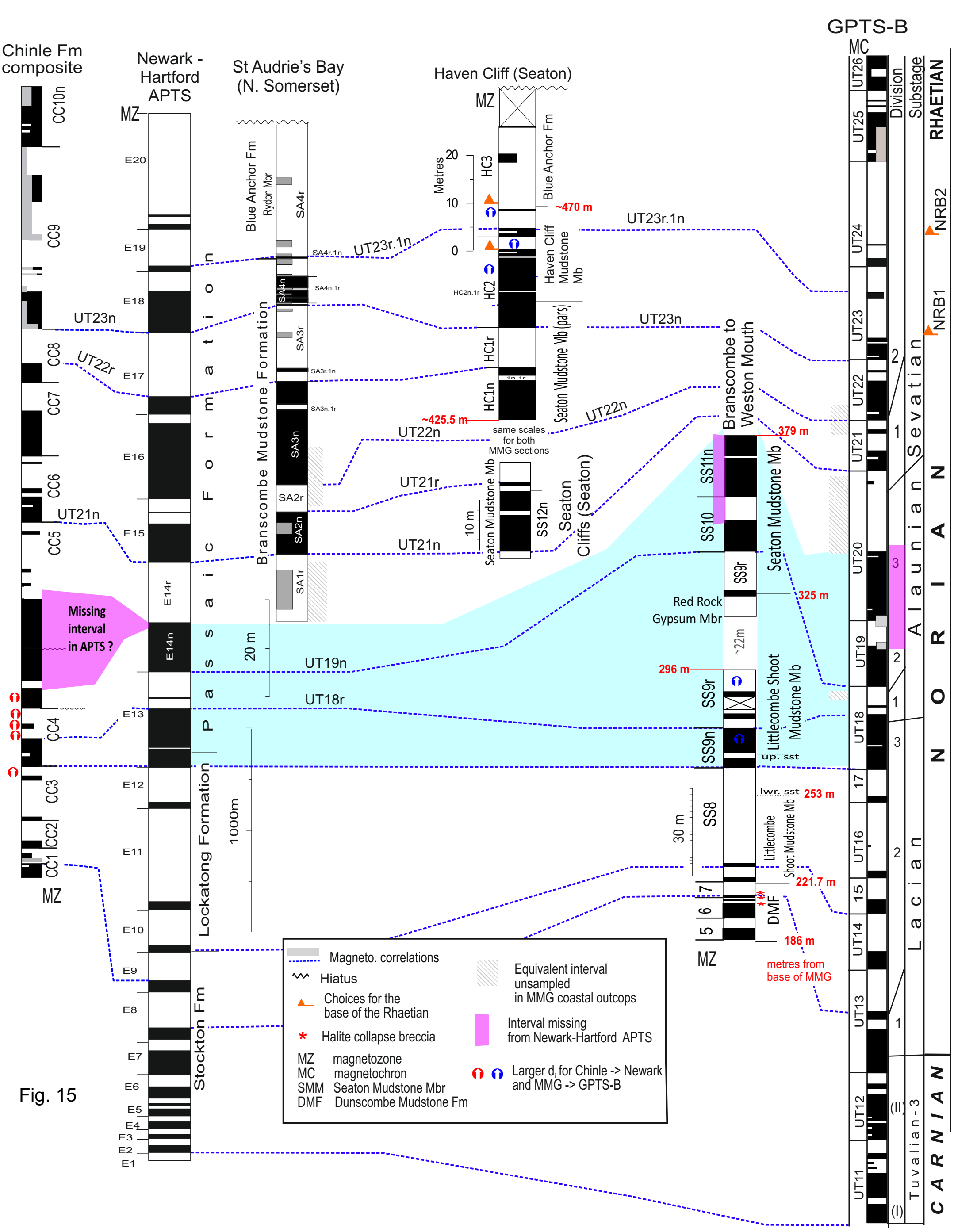
Chinle Fm composite
Newark - Hartford APTS
St Audrie's Bay (N. Somerset)
Haven Cliff (Seaton)
GPTS-B
MC
MZ
CC10n
CC9
CC8
CC7
CC6
CC5
CC4
CC3
CC2
CC1
E20
E19
E18
E17
E16
E15
E14r
E14n
E13
E12
E11
E10
E9
E8
E7
E6
E5
E4
E3
E2
E1
UT23n
UT22r
UT21n
UT23r.1n
UT22n
UT21r
UT19n
UT18r
Passaic Formation
Lockatong Formation
Stockton Fm
1000m
Blue Anchor Fm
Rydon Mbr
SA4r
SA4r.1n
SA4n
SA4n.1r
SA3r
SA3r.1n
SA3n
SA3n.1n
SA2r
SA2n
SA1r
Branscombe Mudstone Formation
20 m
Missing interval in APTS ?
Metres
20
10
0
HC3
HC2
HC2n.1r
HC1r
HC1n
1n.1r
~470 m
~425.5 m
Haven Cliff Mudstone Mb
Seaton Mudstone Mb (pars)
same scales for both MMG sections
Seaton Mudstone Mb
10 m
SS12n
Seaton Cliffs (Seaton)
SS11n
SS10
SS9r
SS9n
SS8
30 m
Red Rock Gypsum Mbr
~22m
296 m
Littlecombe Shoot Mudstone Mb
up. sst
lwr. sst
253 m
221.7 m
DMF
186 m
379 m
Seaton Mudstone Mb
325 m
Branscombe to Weston Mouth
metres from base of MMG
UT26
UT25
UT24
UT23
UT22
UT21
UT20
UT19
UT18
17
UT16
15
UT14
UT13
UT12
UT11
Division
Substage
RHAETIAN
NRB2
NRB1
Alaunian
Sevatian
1
2
3
NORIAN
Lacian
Tuvalian-3
(II)
(I)
CARNIAN
Magneto. correlations
Hiatus
Choices for the base of the Rhaetian
Halite collapse breccia
MZ magnetozone
MC magnetochron
SMM Seaton Mudstone Mbr
DMF Dunscombe Mudstone Fm
Equivalent interval unsampled in MMG coastal outcops
Interval missing from Newark-Hartford APTS
Larger d13C for Chinle -> Newark and MMG -> GPTS-B

Fig. 15

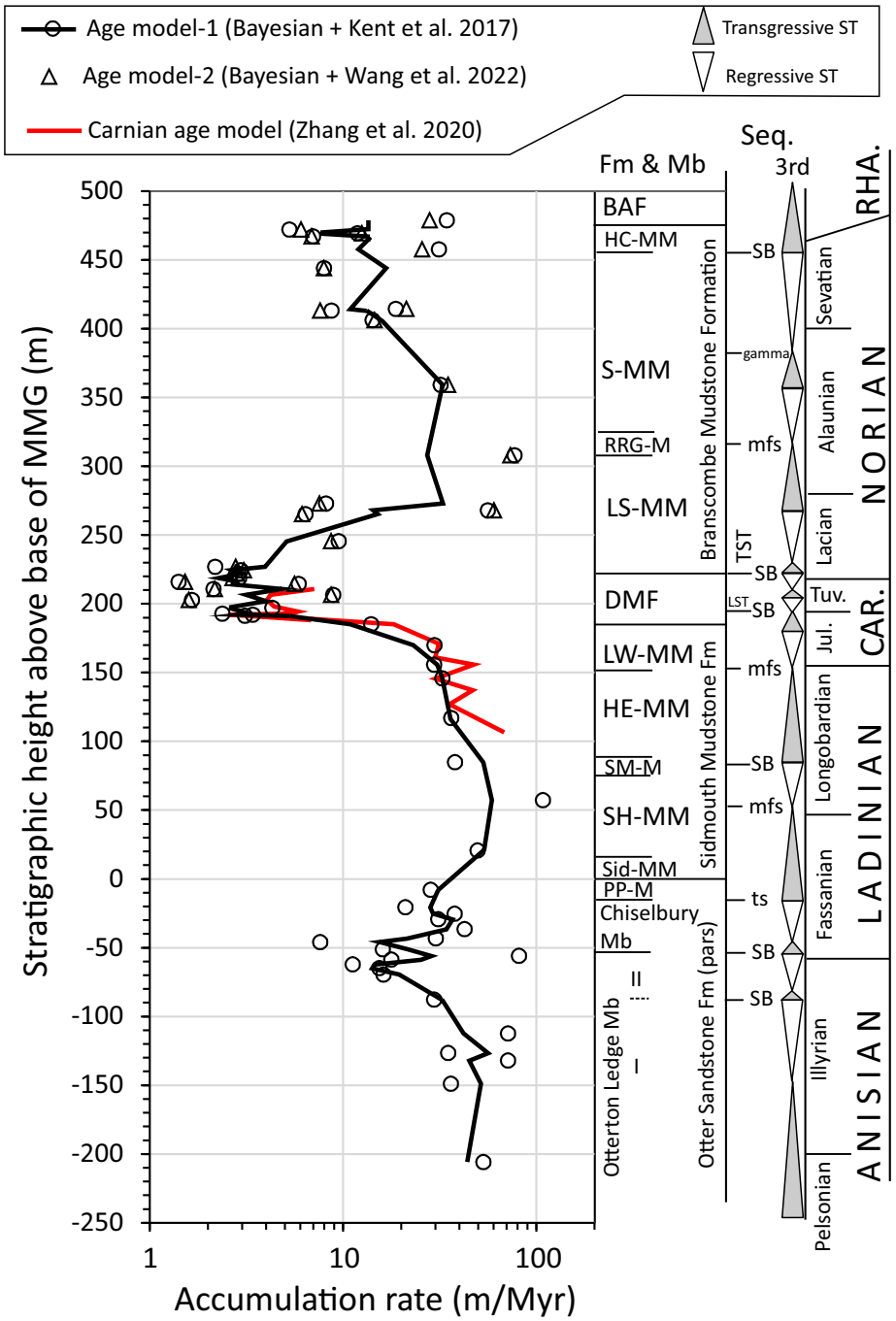
Age model-1 (Bayesian + Kent et al. 2017)
Age model-2 (Bayesian + Wang et al. 2022)
Carnian age model (Zhang et al. 2020)
Transgressive ST
Regressive ST
Stratigraphic height above base of MMG (m)
Accumulation rate (m/Myr)
Fm & Mb
BAF
HC-MM
S-MM
RRG-M
LS-MM
DMF
LW-MM
HE-MM
SM-M
SH-MM
Sid-MM
PP-M
Chiselbury Mb
Otterton Ledge Mb
II
I
Branscombe Mudstone Formation
Sidmouth Mudstone Fm
Otter Sandstone Fm (pars)
Seq.
3rd
SB
gamma
mfs
TST
LST
ts
Sevatian
Alaunian
Lacian
Tuv.
Jul.
Longobardian
Fassanian
Illyrian
Pelsonian
NORIAN
CAR.
LADINIAN
ANISIAN
RHA.

Fig. 16